The Shear Deformation Zone and the Smoothing of Faults with Displacement

Clement Perrin[1], Felix Waldhauser[2], and Christopher H. Scholz[3]

[1]Institut De Physique Du Globe De Paris
[2]Lamont-Doherty Earth Observatory of Columbia University
[3]Lamont-Doherty Earth Observatory

November 26, 2022

Abstract

We use high-resolution earthquake locations to characterize the three-dimensional structure of active faults and how it evolves with fault structural maturity. We investigate the distribution of aftershocks of several recent large earthquakes that occurred on crustal strike slip faults of various structural maturity (i.e. various cumulative fault displacement, length, initiation age and slip rate). Aftershocks define a tabular zone of shear deformation surrounding the mainshock rupture plane. Comparing this to geological observations, we conclude that this results from the re-activation of secondary faults. We observe a rapid fall off of the number of aftershocks at a distance range of 0.06-0.25 km from the main fault surface of mature faults, and 0.7-1.5 km from the fault surface of immature faults. The total width of the active shear deformation zone surrounding the main fault plane reaches ~1.5 km and 2.5-6 km for mature and immature faults, respectively. We find that the width of the shear deformation zone decreases as a power law with cumulative fault displacement. Comparing with an existing dynamic rough fault model, we show that the narrowing of the shear deformation zone agrees quantitatively with earlier estimates of the smoothing of faults with displacement, both of which are aspects of fault wear. We compare this evolution of fault structure with several attributes of earthquakes, and find that earthquake stress drop decreases with fault displacement and hence with increased smoothness.

The Shear Deformation Zone and the Smoothing of Faults with Displacement

Clément Perrin[1,2,*], Felix Waldhauser[1] and Christopher H. Scholz[1]

[1] Lamont Doherty Earth Observatory at Columbia University, New York, USA

[2] Present address: Université de Paris, Institut de physique du globe de Paris, CNRS, F-75005 Paris, France

[*] **Corresponding author: perrin@ipgp.fr**

Keypoints:

Across strike distributions of aftershocks of large earthquakes describe the width of the shear deformation zone around large faults.

The zone of active shear deformation scales with fault roughness and narrows as a power law with fault displacement.

Earthquake stress drop decreases with fault displacement and hence fault roughness.

Keywords:

Fault maturity; shear deformation zone; large earthquakes; aftershock distributions; scaling laws.

Plain Language Summary

Active fault zones worldwide are 3D features made of a parent fault and secondary faults and fractures that damaged the surrounding medium. During and soon after a large earthquake, these structures are reactivated, highlighted by numerous smaller events, also called aftershocks. Their distribution allows us to characterize the zone of shear deformation around the fault plane. In this study, we show that the width of the shear deformation zone is narrower around mature faults than around immature faults. It decreases as a power law with cumulative fault displacement as the result of the smoothing of the fault with wear through geological times. Our study provides some relations to better understand and anticipate the size of off-fault deformation reactivated during and after an earthquake, based on geological fault parameters.

Abstract

We use high-resolution earthquake locations to characterize the three-dimensional structure of active faults and how it evolves with fault structural maturity. We investigate the distribution of aftershocks of several recent large earthquakes that occurred on crustal strike slip faults of various structural maturity (i.e. various cumulative fault displacement, length, initiation age and slip rate). Aftershocks define a tabular zone of shear deformation surrounding the mainshock rupture plane. Comparing this to geological observations, we conclude that this results from the re-activation of secondary faults. We observe a rapid fall off of the number of aftershocks at a distance range of 0.06 – 0.25 km from the main fault surface of mature faults, and 0.7-1.5 km from the fault surface of immature faults. The total width of the active shear deformation zone surrounding the main fault plane reaches ~1.5 km and 2.5-6 km for mature and immature faults, respectively. We find that the width of the shear deformation zone decreases as a power law with cumulative fault displacement. Comparing with an existing dynamic rough fault model, we show that the narrowing of the shear deformation zone agrees quantitatively with earlier estimates of the smoothing of faults with displacement, both of which are aspects of fault wear. We compare this evolution of fault structure with several attributes of earthquakes, and find that earthquake stress drop decreases with fault displacement and hence with increased smoothness.

1. Introduction

A fault zone is a complex brittle-frictional system that wears as slip occurs on it. It is formed of three main features, that will evolve with fault growth (Fig. 1): (i) the cataclastic core contains the cataclastic detritus of wear of the slipping surfaces of the fault. Its width (W_C in Fig. 1) increases linearly with fault displacement at a rate that depends on the strength of the wall rock (Scholz, 1987, 2019, pp 132). For displacements greater than a few hundred meters, growth of the fault core levels off at a thickness of a few tens of meters (Scholz, 2019, pp 132); (ii) Beyond the fault core lies a region of pervasive tensile fracturing which defines the "dilatant damage zone" (W_D, Fig. 1; e.g. Faulkner et al., 2011; Savage & Brodsky, 2011; Vermilye & Scholz, 1998). The fracture density in this zone dies off as a power law with distance from the fault (e.g., Ostermeijer et al., 2020 and references therein). The dilatant damage zone width increases linearly with fault displacement, and typically levels out at several hundred meters for fault displacements exceeding several hundred meters (Savage & Brodsky, 2011); (iii) Including and extending beyond the dilatant damage zone is what we call the "shear deformation zone" (W_S; Fig. 1) which is defined by a region of enhanced seismicity, first pointed out by Powers & Jordan, 2010. This zone shows a region of high activity near the fault with a power law fall-off beyond a corner at W_{S1} to a full half-width of W_{S2} (Fig. 1).

The above definitions allow us to distinguish two types of damage zones: the “dilatant damage zone” dominated by volumetric strains, and the “shear deformation zone” dominated by shear strains. The tensile (Mode I) cracks in the dilatant damage zone are dilatant cracks that align parallel to the maximum compression direction and perpendicular to the minimum principal stress. Hence their orientation provides evidence for the several different mechanisms responsible for them (Wilson et al., 2003). The shear deformation zone is characterized by secondary faults (Mode II and III cracks) and hence are oriented parallel to the maximum Coulomb stress. For example, in the case of a strike-slip fault, this zone is defined by a conjugate set of secondary faults (Little, 1995).

The evolution of these three zones defines what is called fault maturity. The three zones can be viewed as regions controlled by wear processes, and the fault structural maturity can hence be measured by its degree of wear, which depends primarily on the net fault displacement. However, previous studies have shown that, in the absence of data on net fault displacement, several other fault parameters such as the fault initiation age and the geological slip rate can be also used as a proxy of net displacement in evaluating the overall maturity of the fault (e.g. Choy et al., 2006; Choy & Kirby, 2004; Dolan & Haravitch, 2014; Hecker et al., 2010; Ikari et al., 2011; Manighetti et al., 2007; Niemeijer et al., 2010; Perrin et al., 2016a; Stirling et al., 1996; Wesnousky, 1988). As these parameters increase, the fault grows and becomes more “mature”. Prior studies have suggested that the structural maturity may have a strong impact on earthquake behavior, such as magnitude, stress drop, distribution of slip, ground motion amplitude, and number of ruptured segments (e.g., Cao & Aki, 1986; Dolan & Haravitch, 2014; Hecker et al., 2010; Malagnini et al., 2010; Manighetti et al., 2007; Perrin et al., 2016a; Radiguet et al., 2009; Stirling et al., 1996; Wesnousky, 1988).

The widths of the fault core and dilatant damage zones saturate at fault lengths comparable to the seismogenic thickness, so that for large faults, the evolution of fault maturity involves only changes in the shear deformation zone. In this paper we are concerned with the scaling of large faults (i.e. which reach the brittle seismogenic depth) and their associated large earthquakes, so we are only concerned with the shear deformation zone. There is evidence that indicates that large faults become smoother with net displacement (Stirling et al., 1996; Wesnousky, 1988). This smoothing is probably the prime attribute of fault maturity. Here we show that the width of the shear deformation zone of large faults decreases with fault displacement, as a consequence of this smoothing.

Precise earthquake locations can be used to image the internal structure of fault and the zone of brittle deformation, often at a resolution similar to field observations (e.g. Powers & Jordan, 2010; Hauksson, 2010; Valoroso et al., 2014). Powers & Jordan (2010) studied the association of small earthquakes with large faults in California. They found that the frequency of small earthquakes is highest in a narrow region surrounding faults and then falls off as a power law at greater distances. They modeled this behavior with a fault model with rough (fractal) topography (Dieterich & Smith, 2009), showing that such a rough fault model would produce high stresses near the fault that could account for the seismicity. The seismicity they used was from the interseismic period of the faults. Although stacked profiles from many fault sections show the association with the faults, individual sections and map views, both in Powers & Jordan (2010) and Hauksson (2010) show that such a tight correlation with the fault is not typical of individual fault segments, for which a wide variety of distributions of seismicity can be observed. As Hauksson (2010) observed, this variability is likely due to many factors, such as heterogeneity in lithology, the effect of nearby faults both mapped and unmapped, and fault offsets and bends.

As Hauksson (2010) observed further, aftershocks of large earthquakes, in contrast, always show a tight clustering around the main fault. The majority of aftershocks of large earthquakes occur close to the rupture surface, and are often used to delineate it. In an earthquake model with a smooth rupture surface, the near-fault area lies in a deep stress shadow (Kostrov & Das, 1984). Near-fault aftershocks therefore are an indication of a rough fault, as near-fault stresses are generated by dynamic slip on rough topography. They are greatest right after the mainshock, after which they are relaxed by aftershocks and other relaxation mechanisms. In this study, in order to estimate the roughness of active faults, and how they evolve with displacement, we use high-precision aftershock locations of large earthquakes on faults with different net displacements.

2. Data analysis

2.1 High-resolution earthquake location

We use high-resolution earthquake catalogs available in the literature to analyze the aftershock distribution of eight large ($M_w \geq 6$) continental strike slip earthquakes: the 1984 Morgan Hill, 2004 Parkfield, and 2014 South Napa earthquakes in northern and central California (Waldhauser, 2009; Waldhauser & Schaff, 2008), the 1987 Superstition Hills, 1992 Landers, 1999 Hector Mine, and 2010 El Mayor Cucapah earthquakes in Southern California/Mexico (Hauksson et al., 2012), and the 2000 Tottori earthquake in Japan (Fukuyama et al., 2003). These earthquakes were selected because high precision catalogues were available for their aftershocks and because they occurred on faults with a wide range of net displacement. In order to perform an appropriate and homogeneous analysis of all cases, we selected events of Mw>1 within 2 months of each mainshock, all relocated by double difference techniques (Waldhauser & Ellsworth, 2000).

For each aftershock sequence we determine the three-dimensional fault geometry by applying a principal component analysis (PCA) to all events within boxes that are between 3 and 10 km long along strike and between 3 and 20 km wide across strike (i.e. centered on the surface fault trace in map view), stepping at 1 km intervals along the fault trace (Perrin et al., 2019). For each box, we obtain a plane that best fits the locations of aftershocks. For simplicity, we assume, in each box, a constant dip of the calculated planes as a function of depth (see also Perrin et al., 2019). Then we deduce the orthogonal distance between each event and the calculated fault plane segment, and sum up the the number of aftershocks on each side of the fault within bins of 50 m from the fault plane (but 20 m for Parkfield) (gray curves in Fig. 2b, d, e, f, g and Supp. Fig. S1). These gray distributions are normalized by the total number of aftershocks in each box. We use the mean values of the normalized number of events in each bin (black curve in Fig. 2 and Supp. Fig. 1) to describe the smoothed distribution of aftershocks away from the fault plane.

We use two parameters to describe the smoothed near-fault aftershock distribution: the location where the number of events begins to fall off with distance from the fault (W_{S1}), and the location where the background level of seismic activity is reached (W_{S2}). In order to find these parameters we use a power law function to fit the mean normalized aftershock distribution (red fit in Fig. 3 and Supp. Fig. 2) and defined W_{S1} at the location where the function reaches a maximum in its 2nd derivative. W_{S2} corresponds to the distance where the mean distribution departs from the fit (see Fig. 3), as defined also in Powers and Jordan (2010). In a few cases (e.g., Hector Mine, Superstition Hills, Landers), W_{S2} cannot be determined because the background level cannot be estimated due to the presence of subparallel or sub-perpendicular fault sections that bias the number of events. In these cases, we use the W_{S2} values determined from other fault segments that broke during the same earthquake, hence assuming a similar background seismicity level away from the different fault sections.

As an example of our approach, the analyses of the 2004 Parkfield and 1999 Hector Mine aftershocks are presented in figure 2 and 3 (see Supp. Fig. S1 and S2 for all earthquake cases). The near-fault aftershock distribution at Parkfield (black curve, Fig. 3a) describes a rapid fall off at ~0.06 km away from the fault plane (W_{S1}) until they reach background seismicity levels at ~0.8 km from the fault plane (W_{S2}). In cases with multiple rupture traces (i.e. Hector Mine, Landers, El Mayor Cucapah), we separately analyzed each main section that broke during the earthquake (Fig. 2c, d, e, f, g, 3b, c, d, e and Supp. Fig. S1 and S2). In these cases, the aftershocks distributions were fairly similar for the different traces. Hence, we averaged W_{S1} and W_{S2}, when possible, so that single values could be assigned to each earthquake sequence. Table 1 lists measurements for the eight earthquakes analyzed in this study.

Also listed in Table 1 are data from the Awatere fault. This right-lateral strike-slip fault is a first order splay of the Alpine fault of New Zealand. It crosses the coast at a sea-cliff that offers an almost complete exposure of the entire fault zone from the fault core through the shear deformation zone. This was mapped by Little (1995), who showed that the shear deformation zone consists of a set of conjugate strike-slip secondary faults that decreased in frequency with distance from the primary fault in the same manner as the aftershocks do in our study. The right-lateral set of the secondary faults is nearly sub-parallel to the main fault and the left-lateral set about 60° from that. Values of W_{S1} and W_{S2} obtained from that data are indicated in Table 1. An exposure at mid-crustal depths of a strike-slip fault in Austria shows just the same orientation of secondary faults (Frost et al., 2009). These observations provide the 'ground truth' for the structures upon which the near-fault aftershocks occur.

2.2 Fault parameters

We collect key parameters describing the degree of evolution of the faults that broke during the selected earthquakes. Since faults propagate laterally through time, their structural maturity varies also along strike (Perrin et al., 2016a; 2016b). Thus, it is necessary to use fault parameters that describe the local fault maturity where the rupture occurred. This is particularly true for long faults, such as the San Andreas Fault, for which fault initiation age varies greatly along the fault, from ancient fault sections in Central California (24 to 29 Ma at Parkfield; e.g. Atwater & Stock, 1998; Liu et al., 2010) to younger fault sections in Southern California (<12Ma, e.g. Powell & Weldon, 1992; Sims, 1993), and therefore have different local net displacements. Table 1 presents the fault parameters used in this study. The eight fault sections span a wide range of structural maturity, with various initiation ages (1.1 to 29 Ma), cumulative displacements (1 to 315 km) and geological slip rates (0.1 to 26 mm/yr).

In the case of the Tottori earthquake the cumulative displacement of the Komachi-Odani fault is not known. We estimated it based on the empirical relation from Schlische et al. (1996) that shows that crustal fault displacement scales with their length as $2x10^{-2}$ to $8x10^{-2}$. If we take the fault length from the aftershocks distribution (Fukuyama et al., 2003) to be 35 km, this would give a cumulative displacement in the range 0.7 to 2.8 km (Table 1). In the case of the Awatere fault we do not have aftershock locations, but indstead use the width of the shear deformation zone as inferred from field data measured by Little (1995) across an immature section of the Awatere fault zone, in New Zealand (cumulative slip : < 2±1 km, initiation age : < 4±1 My, long-term slip rate : 5±1 mm/yr near its northeastern tip; Little, 1995 and references therein).

3. Results

We investigate the relationship between the two independent datasets: the aftershock distributions and the fault parameters (Table 1). Our first observation is that W_{S1} (i.e. the half distance from the calculated fault plane where the aftershock rate saturates) and W_{S2} (i.e. the full half-width of the shear deformation zone) correlate with each other (Fig. 4), indicating that these two parameters are not independent and that the shape of the shear deformation zone grows in a self-similar way (although there is an indication that W_{S1} becomes relatively narrower for more mature faults). Figure 5 represents the evolution of the width of the shear deformation zone (i.e. W_{S1} and W_{S2}) as a function of the cumulative fault slip (Fig. 5a and 5b, respectively). Both plots show the same trend: the width of the shear deformation zone, measured with both parameters, decreases with net displacement as a power law with an exponent of -0.55 and -0.35 for W_{S1} and W_{S2}, respectively. These results indicate that the two parameters W_{S1} and W_{S2} scale similarly with displacement.

Note that the field measurements across the Awatere fault (red symbol in Fig. 5) are in good agreement with the trends highlighted from seismological data. This supports the interpretation that the shear deformation zone defined by the width of the aftershock zone corresponds to the width of the zone of active secondary faulting.

As W_{S1} and W_{S2} are found to decrease with cumulative displacement, we observe a similar decrease of these parameters with fault initiation age and slip rate, showing a wider shear deformation zone for younger fault sections (Supp. Fig. S3) and smaller geological slip rates (Supp. Fig. S4), also in good agreement with geological observations across the Awatere fault.

Figure 6a shows the near-fault aftershock distribution as a function of fault perpendicular distance for the eight earthquake sequences considered in this study (see also black curves in Fig. 2 and Supp. Fig. S1). These distributions show a clear pattern: mature fault sections (warm colors in fig. 6a, b and c) are characterized by aftershocks concentrated mainly close to the fault plane. The rapid fall-off in activity away from the fault plane describes a narrow deformation zone at the scale of hundreds of meters. In contrast, immature faults (cold colors in fig. 6a, b and c) exhibit a wider deformation zone at the kilometer scale where events are more widely distributed within the surrounding medium (i.e. lower maximum number of events in the near-field of immature faults than of mature fault sections; fig. 6a and b). The distributions remain proportional to one another, indicating the shape of the shear deformation zone remains constant. Here again, field measurements of cumulative number of faults across the Awatere fault (black squares, fig. 6a; Little, 1995) show a similar trend and corroborate our seismological observations.

4. Discussion

4.1. The Nature of the Shear Deformation Zone and the Smoothing of Faults

In this study we show that for fault displacements greater than 1 km the width of the shear deformation zone, defined by W_{S1} and W_{S2}, decreases with fault displacement. So, what determines the width of the zone of near-fault aftershocks? Models of a mainshock employing smooth faults would indicate a deep stress shadow in this area, precluding the presence of such near-fault aftershocks (Kostrov & Das, 1984). On the other hand, models with rough faults predict high stresses within a well-defined region close to the fault, which corresponds to the shear deformation zone. Powers & Jordan (2010) interpreted their data in just that way, using a rough static fault model of Dieterich & Smith (2009).

Here we consider the model of Aslam & Daub (2018) which calculates the stresses resulting from dynamic ruptures propagating on a rough surface. They characterized the fault as a self-affine fractal with Hurst exponent H and roughness measured by the RMS height to wavelength ratio. This is a fairly realistic rendition of the observed topography of faults (e.g. Candela et al., 2012). Their model predicts large changes in the Coulomb Failure Function (CFF= $\tau + \mu\sigma$), within a well-defined narrow region close to the fault. The receiver faults they assumed are parallel to the primary fault: this would be consistent with the orientation of the secondary faults observed by Little (1995) and

Frost et al. (2009). They find that the width of this near-fault region of high stresses is insensitive to H but decreases as the RMS roughness decreases. If we identify our observed shear deformation zone with that near-fault region of high stresses, this indicates that the observed decrease of W_{S2} with fault displacement is the result of smoothing of the fault with slip.

Aslam & Daub (2018) found that the half width of the near fault zone is ~ 2.7 and ~ 0.9 km for fault profiles with RMS height to wavelength ratios of 0.01 and 0.001, respectively. Comparing these results with the range of W_{S2} in figure 5 indicates that more than an order of magnitude of roughness change will be required to explain these observations. This indicates a wear rate far greater than that which occurs for the roughness of individual fault segments (Brodsky et al., 2011). However, faults are composed of many segments or sub-faults at many scales (Ferrill et al., 1999; Klinger, 2010; Manighetti et al., 2015; Scholz, 1998) and of nested sub-faults offset from one another (Ben-Zion & Sammis, 2003; de Joussineau & Aydin, 2009; Segall & Pollard, 1980). The length distribution of sub-faults follows a power law (Scholz, 1998) and they are offset by jogs that are self-similar (de Joussineau & Aydin, 2009). It therefore would be possible that this combination would produce a fractal topography at a hierarchy higher than that of the roughness of the individual sub-fault.

Geological observations indicate that fault roughness, as measured by segment offsets, decreases with fault slip (de Joussineau & Aydin, 2009; Stirling et al., 1996; Wesnousky, 1988). Stirling et al. (1996) show an approximately linear reduction of fault roughness, measured as segments per unit of fault length, with fault displacement. If we make the reasonable assumption that the fault jog offsets identified by Stirling et al are of order 1 km then the height to wavelength ratios of 0.001 and 0.01 correspond to fault displacements of 100 and 10 km, respectively. Combining these with the corresponding deformation zone widths of Aslam & Daub (2018) give the two data points in Figure 7. The solid black line there is the best fit of the data for W_{S2} from Figure 5b. The excellent agreement confirms the hypothesis that narrowing of the shear deformation zone with fault displacement is the consequence of the smoothing of the fault with wear.

4.2. Relations of Earthquake Parameters with Fault Maturity

The primary feature of the maturation of faults is that their surfaces become smoother with displacement through the process of frictional wear. It might also be supposed that the characteristics of earthquakes may differ according to the maturity of the fault upon which they occur. It has been suggested, for example, that earthquake stress drop, apparent stress, and radiation efficiency vary with fault maturity (Choy et al., 2006; Hecker et al., 2010; Ross et al., 2018). These are not entirely independent parameters. The radiation efficiency, η_R, is given by:

(1) $$\eta_R = \frac{E_R}{E_R+E_G} = \frac{2\mu E_R}{\Delta\sigma M_0} = \frac{2\sigma_a}{\Delta\sigma}$$

where E_R is radiated energy, E_G is the energy dissipated in damage of various types, $\Delta\sigma$ is stress drop, σ_a is apparent stress, M_0 is seismic moment, and μ is the shear modulus. Table 2 gathers these parameters for four earthquakes we have studied and for which this information was available in the literature. Although this list is short, it is expansive, in the sense that it covers four orders of magnitude in fault displacement, which give us the opportunity to test the different hypothesis.

The idea that radiation efficiency increases with fault maturity was based entirely on a comparison of the Tottori and Parkfield earthquakes (Ross et al., 2018). The other two earthquakes in our collection do not support that contention. Our data also do not support the claim of Choy et al. (2006) that apparent stress decreases with fault maturity (Table 2). Their definition of maturity was qualitative and compared faults in different tectonic settings and lithologies. For example, their highest apparent stress was for intraplate oceanic strike-slip faults, and the lowest for subduction zone thrusts. The latter must have a much greater net displacement than the former and hence must be much more mature. However, McGarr (1999) and Choy & McGarr (2002) argue that apparent stress is proportional to strength. If they are correct, then the strength of the oceanic lithosphere, being much greater than the clay-rich and over-pressured oceanic sediments that coat the frictional interface of subduction megathrusts, results in a correspondingly higher apparent stress. The earthquakes in our Table 2, on the other hand, are all strike-slip continental earthquakes so their lithologies are comparable and the variables strength and maturity have been separated so that we can reach a clearer conclusion regarding the effect of maturity on apparent stress.

Hecker et al. (2010) measured the maximum slip to length ratio of prehistoric earthquake scarps on intraplate dip-slip faults in the western U.S. They found that this ratio, an indicator of stress drop, tends to decrease with net fault displacement. Our data is consistent with this finding: figure 8 presents the stress drop ($\Delta\sigma$) as a function of the fault cumulative displacement (D), and show that $\Delta\sigma \propto D^{-0.45}$. Combining this result with our earlier finding that $W_{S2} \propto D^{-0.35}$ implies that $\Delta\sigma \propto W_{S2}$ and hence is linearly proportional to the mean fault roughness, as measured as RMS height to wavelength ratio.

The secondary faults that form the framework of the shear deformation zone must be formed early in the process, when the primary fault is very immature. They are subsequently reactivated by aftershocks in a halo around the fault that gradually narrows as the fault topography smooths with wear (fig. 6). In the early, fault-forming stage, E_G must be much larger relative to E_R and hence η_R will be much smaller than at later stages (Scholz, 2019 pp 137). This might explain the low value of η_R in the Tottori case as compared to earthquakes in later stages.

4.3. Fault Structure and Aftershock Distributions: Strength and Limitations of our Study.

As mentioned earlier, Powers & Jordan (2010) estimated the normal distance of the seismicity away from a signle vertical fault plane inferred from the surface trace of the fault. They defined the zone of shear deformation from the near fault seismicity during the interseismic period and averaged over the entire fault length, possibly neglecting local variations in fault plane orientation and leading to wider zones as compared to our results. In addition, geological heterogeneity and other effects may play a role, as pointed out by Hauksson (2010).

Our approach of fitting only one fault plane to the local aftershock distribution as we step along the fault assumes that the rupture occurred mainly on one fault strand and that aftershocks are homogeneously distributed in the medium around. While individual secondary faults can be clearly distinguished around mature fault sections (see for instance oblique linear streaks around Morgan hill in Supp. Fig. S1), it is more difficult to identify them around immature fault sections (scattered aftershock distribution; i.e. Hector Mine, Landers; Supp. Fig. S1). Yukutake & Iio (2017), for example, analyzed each identifiable secondary strand associated with the main Komachi-Odani fault that broke during the 2000 Tottori earthquake and found smaller across-strike distance for each of them. Moreover, fault zone architectures worldwide are complex and not necessarily symmetrical, especially near their propagating fault tip where secondary faults can be observed on one side of the primary fault (e.g., Perrin et al., 2016b). We do not depict this complexity in our study and simplify it as we sum the number of events on each side of the best fitting plane. However, the seismic signature of secondary faults is included in our smoothed across-strike distributions, which allow us to highlight the overall volume around immature fault zones which is involved in the rupture during earthquakes such as Hector Mine, Landers, Tottori, El Mayor Cucapah and Superstition Hills.

In our study we compare an averaged normal distribution of aftershocks with fault parameters, considering for each case a homogeneous local fault structural maturity along the entire rupture length. But it has been shown that the fault maturity can vary along strike and this can affect the heterogeneity of fracture density around the fault core (Ostermeijer et al., 2020), the distribution of secondary faults at greater distances away from the fault (Perrin et al., 2016b) and finally the behavior of earthquakes (e.g., Huang, 2018; Perrin et al., 2016a). Consequently, it is possible that for long earthquake ruptures or multiple broken faults scenarii, the normal distribution of aftershocks can change along strike, following locally a similar trend (i.e. a wider shear deformation zone in the most immature parts of the rupture) at a local scale that we observe in our study at greater scales. This would be in good agreement with mapped faults at the surface that shows that the off-fault damage zone widens in the direction of long-term fault propagation (e.g., Manighetti et al., 2001; Perrin et al., 2016b). Future work is needed to relate such observations to the occurrence of seismicity.

5. Conclusion

Our study presents strong correlations between independent datasets, i.e. the near-fault distribution of aftershocks following large earthquakes and the associated geological parameters of the long-term faults involved in the rupture (cumulative displacement, initiation age, slip rate). We find that for large faults, defined as those that have ruptured the entire brittle thickness, the zone of active shear deformation narrows as a power law with fault displacement, hence with fault maturity. This result is predicted by a dynamic rough fault model in which fault roughness decreases with displacement. We find that earthquake stress-drop also decreases with fault displacement and hence fault roughness. Our relations show how the volume around fault zones can be reactivated during large earthquakes, depending on fault maturity (i.e. its degree of wear approached here by fault cumulative displacement). Our study can be useful to anticipate across-strike distributions of aftershocks around major fault zones which are not covered by a dense seismic network, based on known geological fault parameters.

ACKNOWLEDMENTS

This work is supported by the Brinson Foundation (CP) and the National Science Foundation (NSF-EAR #1520680). Earthquake catalog data are available at http://ddrt.ldeo.columbia.edu and https://scedc.caltech.edu/research-tools/altcatalogs.html. This paper is LDEO contribution XXX and IPGP contribution XXX.

REFERENCES

Aslam, K. S., & Daub, E. G. (2018). Effect of Fault Roughness on Aftershock Distribution: Elastic Off-Fault Material Properties. *Journal of Geophysical Research: Solid Earth*, *123*(11), 9689–9711. https://doi.org/10.1029/2018JB016214

Atwater, T., & Stock, J. (1998). Pacific North America plate tectonics of the Neogene southwestern United States: An update. *International Geology Review*, *40(5)*, 375–402.

Ben-Zion, Y., & Sammis, C. G. (2003). Characterization of Fault Zones. *Pure and Applied Geophysics*, *160*(3), 677–715. https://doi.org/10.1007/PL00012554

Blisniuk, K., Rockwell, T., Owen, L. A., Oskin, M., Lippincott, C., Caffee, M. W., & Dortch, J. (2010). Late Quaternary slip rate gradient defined using high-resolution topography and ^{10}Be dating of offset landforms on the southern San Jacinto Fault zone, California. *Journal of Geophysical Research: Solid Earth*, *115*(8). https://doi.org/10.1029/2009JB006346

Brodsky, E. E., Gilchrist, J. J., Sagy, A., & Collettini, C. (2011). Faults smooth gradually as a function of slip. *Earth and Planetary Science Letters*, *302*(1–2), 185–193. https://doi.org/10.1016/j.epsl.2010.12.010

Candela, T., Renard, F., Klinger, Y., Mair, K., Schmittbuhl, J., & Brodsky, E. E. (2012). Roughness of fault surfaces over nine decades of length scales. *Journal of Geophysical Research: Solid Earth*, *117*(8), 1–30. https://doi.org/10.1029/2011JB009041

Cao, T., & Aki, K. (1986). Seismicity simulation with a rate- and state-dependent friction law. *Pure and Applied Geophysics*, *124*(3), 487–513. https://doi.org/10.1007/BF00877213

Choy, G. L., & Kirby, S. H. (2004). Apparent stress, fault maturity and seismic hazard for normal-fault earthquakes at subduction zones. *Geophysical Journal International*, *159*(3), 991–1012. https://doi.org/10.1111/j.1365-246X.2004.02449.x

Choy, G. L., & McGarr, A. (2002). Strike-slip earthquakes in the oceanic lithosphere: observations of exceptionally high apparent stress. *Geophysical Journal International*, *150*(2), 506–523. https://doi.org/10.1046/j.1365-246X.2002.01720.x

Choy, G. L., McGarr, A., Kirby, S. H., & Boatwright, J. (2006). An overview of the global variability in radiated energy and apparent stress. In R. Abercrombie & E. Al. (Eds.), *Geophysical Monograph Series* (pp. 43–57). Washington DC: AGU. https://doi.org/10.1029/170GM06

Critelli, S., & Nilsen, T. H. (2000). Provenance and stratigraphy of the Eocene Tejon Formation, Western Tehachapi Mountains, San Emigdio Mountains, and Southern San Joaquin Basin, California. *Sedimentary Geology*, *136*, 7–27.

Crowell, J. C. (1979). The San Andreas fault system through time. *Journal of the Geological Society*, *136*, 293–302. https://doi.org/10.1144/gsjgs.136.3.0293

Dibblee, T. W. J. (1961). Evidence of strike-slip movement on northwest-trending faults in the western Mojave Desert, California. *U.S. Geological Survey Professional Paper*, *424-B*, B197–B199.

Dieterich, J. H., & Smith, D. E. (2009). Nonplanar faults: Mechanics of slip and off-fault damage. *Pure and Applied Geophysics*, *166*, 1799–1815. https://doi.org/10.1007/s00024-009-0517-y

Dokka, R. K. (1983). Geology Displacements on late Cenozoic strike-slip faults of the central Mojave Desert, California Displacements on late Cenozoic strike-slip faults of the central Mojave Desert, California, (May), 305–308. https://doi.org/10.1130/0091-7613(1983)11<305

Dokka, R. K., & Travis, C. J. (1990). Late Cenozoic strike-slip faulting in the Mojave

Desert, California. *Tectonics*. https://doi.org/10.1029/TC009i002p00311

Dolan, J. F., & Haravitch, B. D. (2014). How well do surface slip measurements track slip at depth in large strike-slip earthquakes? The importance of fault structural maturity in controlling on-fault slip versus off-fault surface deformation. *Earth and Planetary Science Letters*, *388*(C), 38–47. https://doi.org/10.1016/j.epsl.2013.11.043

Dorsey, R. J., Axen, G. J., Peryam, T. C., & Kairouz, M. E. (2012). Initiation of the southern Elsinore fault at ~1.2 Ma: Evidence from the Fish Creek-Vallecito Basin, southern California. *Tectonics*, *31*(2), 1–21. https://doi.org/10.1029/2011TC003009

Faulkner, D. R., Mitchell, T. M., Jensen, E., & Cembrano, J. (2011). Scaling of fault damage zones with displacement and the implications for fault growth processes. *Journal of Geophysical Research: Solid Earth*, *116*(5), 1–11. https://doi.org/10.1029/2010JB007788

Ferrill, D. A., Stamatakos, J. A., & Sims, D. W. (1999). Normal fault corrugation: Implications for growth and seismicity of active normal faults. *Journal of Structural Geology*, *21*, 1027–1038. https://doi.org/10.1016/S0191-8141(99)00017-6

Fletcher, J. B., & McGarr, A. (2006). Distribution of stress drop, stiffness, and fracture energy over earthquake rupture zones. *Journal of Geophysical Research: Solid Earth*, *111*(B3), n/a-n/a. https://doi.org/10.1029/2004JB003396

Fletcher, K. E. K., Rockwell, T. K., & Sharp, W. D. (2011). Late Quaternary slip rate of the southern Elsinore fault, Southern California: Dating offset alluvial fans via ^{230}Th/U on pedogenic carbonate. *Journal of Geophysical Research: Earth Surface*, *116*(2). https://doi.org/10.1029/2010JF001701

Frost, E., Dolan, J., Sammis, C., Hacker, B., Cole, J., & Ratschbacher, L. (2009). Progressive strain localization in a major strike-slip fault exhumed from midseismogenic depths: Structural observations from the Salzach-Ennstal-Mariazell-Puchberg fault system, Austria. *Journal of Geophysical Research*, *114*(B4), B04406. https://doi.org/10.1029/2008JB005763

Fukuyama, E., Ellsworth, W. L., Waldhauser, F., & Kubo, A. (2003). Detailed Fault Structure of the 2000 Western Tottori , Japan , Earthquake Sequence. *Bulletin of the Seismological Society of America*, *93*(4), 1468–1478. https://doi.org/10.1785/0120020123

Garfunkel, Z. (1974). Model for the Late Cenozoic Tectonic History of the Mojave Desert , California , and for Its Relation to Adjacent Regions. *Bulletin of the Geological Society of America*, *85*(December), 1931. https://doi.org/10.1130/0016-7606(1974)85<1931

Graham, S. A., Stanley, R. G., Bent, J. V., & Carter, J. B. (1989). Oligocene and Miocene paleogeography of central California and displacement along the San Andreas fault. *Geological Society of America Bulletin*, *101*, 711–730.

Gurrola, L. D., & Rockwell, T. K. (1996). Timing and slip for prehistoric earthquakes on the Superstition Mountain Fault, Imperial Valley, southern California. *Journal of Geophysical Research: Solid Earth*, *101*(B3), 5977–5985. https://doi.org/10.1029/95JB03061

Hauksson, E. (2010). Spatial Separation of Large Earthquakes, Aftershocks, and Background Seismicity: Analysis of Interseismic and Coseismic Seismicity Patterns in Southern California. *Pure and Applied Geophysics*, *167*(8–9), 979–997. https://doi.org/10.1007/s00024-010-0083-3

Hauksson, E., Yang, W., & Shearer, P. M. (2012). Waveform relocated earthquake catalog for Southern California (1981 to June 2011). *Bulletin of the Seismological Society of America*, *102*(5), 2239–2244. https://doi.org/10.1785/0120120010

Hecker, S., Dawson, T. E., & Schwartz, D. P. (2010). Normal-Faulting Slip Maxima and Stress-Drop Variability: A Geological Perspective. *Bulletin of the Seismological Society of America*, *100*(6), 3130–3147. https://doi.org/10.1785/0120090356

Huang, Y. (2018). Earthquake Rupture in Fault Zones With Along-Strike Material Heterogeneity. *Journal of Geophysical Research: Solid Earth*, *123*(11), 9884–9898. https://doi.org/10.1029/2018JB016354

Hudnut, K. W., & Sieh, K. (1989). Behavior of the Superstition Hills fault during the past 330 years. *Bulletin of the Seismological Society of America*, *79*(2), 304–329.

Ikari, M. J., Marone, C., & Saffer, D. M. (2011). On the relation between fault strength and frictional stability. *Geology*, *39*(1), 83–86. https://doi.org/10.1130/G31416.1

Jachens, R. C., Langenheim, V. E., & Matti, J. C. (2002). Relationship of the 1999 Hector Mine and 1992 Landers fault ruptures to offsets on neogene faults and distribution of late Cenozoic basins in the eastern California shear zone. *Bulletin of the Seismological Society of America*, *92*(4), 1592–1605. https://doi.org/10.1785/0120000915

de Joussineau, G., & Aydin, A. (2009). Segmentation along strike-slip faults revisited. *Pure and Applied Geophysics*, *166*(10–11), 1575–1594. https://doi.org/10.1007/s00024-009-0511-4

Kaverina, A. (2002). The Combined Inversion of Seismic and Geodetic Data for the Source Process of the 16 October 1999 Mw 7.1 Hector Mine, California, Earthquake. *Bulletin of the Seismological Society of America*, *92*(4), 1266–1280. https://doi.org/10.1785/0120000907

Kim, A., & Dreger, D. S. (2008). Rupture process of the 2004 Parkfield earthquake from near-fault seismic waveform and geodetic records. *Journal of Geophysical Research*, *113*(B7), B07308. https://doi.org/10.1029/2007JB005115

Kirby, S. M., Janecke, S. U., Dorsey, R. J., Housen, B. A., Langenheim, V. E., McDougall, K. A., & Steely, A. N. (2007). Pleistocene brawley and ocotillo formations: Evidence for initial strike-slip deformation along the San Felipe and San Jacinto fault zones, southern California. *Journal of Geology*, *115*(1), 42–62. https://doi.org/10.1086/509248

Klinger, Y. (2010). Relation between continental strike-slip earthquake segmentation and thickness of the crust. *Journal of Geophysical Research*, *115*(B7), B07306. https://doi.org/10.1029/2009JB006550

Kostrov, B. V., & Das, S. (1984). Evaluation of stress and displacement fields due to an elliptical plane shear crack. *Geophysical Journal International*, *78*(1), 19–33. https://doi.org/10.1111/j.1365-246X.1984.tb06469.x

Little, T. A. (1995). Brittle deformation adjacent to the Awatere strike-slip fault in New Zealand: Faulting patterns, scaling relationships, and displacement partitioning. *Geological Society of America Bulletin*, *107*(11), 1255–1271. https://doi.org/10.1130/0016-7606(1995)107<1255:BDATTA>2.3.CO;2

Liu, M., Wang, H., & Li, Q. (2010). Inception of the eastern California shear zone and evolution of the Pacific-North American plate boundary: From kinematics to geodynamics. *Journal of Geophysical Research*, *115*(B7), B07401. https://doi.org/10.1029/2009JB007055

Lutz, A. T., Dorsey, R. J., Housen, B. A., & Janecke, S. U. (2006). Stratigraphic record of Pleistocene faulting and basin evolution in the Borrego Badlands, San Jacinto fault zone, Southern California. *Bulletin of the Geological Society of America*, *118*(11–12), 1377–1397. https://doi.org/10.1130/B25946.1

Ma, S., Custódio, S., Archuleta, R. J., & Liu, P. (2008). Dynamic modeling of the 2004 Mw 6.0 Parkfield, California, earthquake. *Journal of Geophysical Research: Solid Earth*, *113*(2), 1–16. https://doi.org/10.1029/2007JB005216

Malagnini, L., Nielsen, S., Mayeda, K., & Boschi, E. (2010). Energy radiation from intermediate- to large-magnitude earthquakes: Implications for dynamic fault weakening. *Journal of Geophysical Research: Solid Earth*, *115*, 1–30. https://doi.org/10.1029/2009JB006786

Manighetti, I., King, G. C. P., Gaudemer, Y., Scholz, C. H., & Doubre, C. (2001). Slip accumulation and lateral propagation of active normal faults in Afar. *Journal of Geophysical Research*, *106*(B7), 13667. https://doi.org/10.1029/2000JB900471

Manighetti, I., Campillo, M., Bouley, S., & Cotton, F. (2007). Earthquake scaling, fault segmentation, and structural maturity. *Earth and Planetary Science Letters*, *253*(3–4), 429–438. https://doi.org/10.1016/j.epsl.2006.11.004

Manighetti, I., Caulet, C., De Barros, D., Perrin, C., Cappa, F., & Gaudemer, Y. (2015). Generic along-strike segmentation of Afar normal faults, East Africa: Implications on fault growth and stress heterogeneity on seismogenic fault planes. *Geochem. Geophys. Geosyst.*, *16*, 443–467. https://doi.org/10.1002/2014GC005691.Received

Matthews, V. (1976). Correlation of Pinnacles and Neenach volcanic formations and their bearing on San Andreas fault problem. *The American Association of Petroleum Geologists Bulletin*, *60*, 2128–2141.

McGarr, A. (1999). On relating apparent stress to the stress causing earthquake fault slip. *Journal of Geophysical Research: Solid Earth*, *104*(B2), 3003–3011. https://doi.org/10.1029/1998JB900083

Niemeijer, A. R., Marone, C., & Elsworth, D. (2010). Fabric induced weakness of tectonic faults. *Geophysical Research Letters*, *37*(3), n/a-n/a. https://doi.org/10.1029/2009GL041689

Oskin, M., Perg, L., Blumentritt, D., Mukhopadhyay, S., & Iriondo, A. (2007). Slip rate of the Calico fault: Implications for geologic versus geodetic rate discrepancy in the Eastern California Shear Zone. *Journal of Geophysical Research: Solid Earth*, *112*(3), 1–16. https://doi.org/10.1029/2006JB004451

Ostermeijer, G. A., Mitchell, T. M., Aben, F. M., Dorsey, M. T., Browning, J., Rockwell, T. K., et al. (2020). Damage zone heterogeneity on seismogenic faults in crystalline rock; a field study of the Borrego Fault, Baja California. *Journal of Structural Geology*, 104016. https://doi.org/10.1016/j.jsg.2020.104016

Perrin, C., Manighetti, I., Ampuero, J.-P., Cappa, F., & Gaudemer, Y. (2016). Location of largest earthquake slip and fast rupture controlled by along-strike change in fault structural maturity due to fault growth. *Journal of Geophysical Research: Solid Earth*, *121*(5), 3666–3685. https://doi.org/10.1002/2015JB012671

Perrin, C., Manighetti, I., & Gaudemer, Y. (2016). Off-fault tip splay networks: A genetic and generic property of faults indicative of their long-term propagation. *Comptes Rendus Geoscience*, *348*(1), 52–60. https://doi.org/10.1016/j.crte.2015.05.002

Perrin, C., Waldhauser, F., Choi, E., & Scholz, C. H. (2019). Persistent fine-scale fault structure and rupture development: A new twist in the Parkfield, California, story. *Earth and Planetary Science Letters*, *521*, 128–138. https://doi.org/10.1016/j.epsl.2019.06.010

Powell, R. E., & Weldon, R. J. (1992). Evolution of the San Andreas Fault. *Annual Review of Earth and Planetary Sciences*, *20*(1), 431–468. https://doi.org/10.1146/annurev.ea.20.050192.002243

Powers, P. M., & Jordan, T. H. (2010). Distribution of seismicity across strike-slip faults in California. *Journal of Geophysical Research: Solid Earth*, *115*(5). https://doi.org/10.1029/2008JB006234

Radiguet, M., Cotton, F., Manighetti, I., Campillo, M., & Douglas, J. (2009). Dependency of

Near-Field Ground Motions on the Structural Maturity of the Ruptured Faults. *Bulletin of the Seismological Society of America*, *99*(4), 2572–2581. https://doi.org/10.1785/0120080340

Revenaugh, J., & Reasoner, C. (1997). Cumulative offset of the San Andreas fault in central California: A seismic approach. *Geology*, *25*(2), 123–126. https://doi.org/10.1130/0091-7613(1997)025<0123:COOTSA>2.3.CO;2

Rockwell, T. K., Lindvall, S., Herzberg, M., Murbach, D., Dawson, T., & Berger, G. (2000). Paleoseismology of the Johnson Valley, Kickapoo, and Homestead Valley faults: Clustering of earthquakes in the Eastern California shear zone. *Bulletin of the Seismological Society of America*, *90*(5), 1200–1236. https://doi.org/10.1785/0119990023

Ross, Z. E., Kanamori, H., Hauksson, E., & Aso, N. (2018). Dissipative Intraplate Faulting During the 2016 Mw 6.2 Tottori, Japan Earthquake. *Journal of Geophysical Research: Solid Earth*, *123*(2), 1631–1642. https://doi.org/10.1002/2017JB015077

Rubin, C. M., & Sieh, K. (1997). Long dormancy, low slip rate, and similar slip-per-event for the Emerson fault, eastern California shear zone. *Journal of Geophysical Research*, *102*(B7), 15319. https://doi.org/10.1029/97JB00265

Savage, H. M., & Brodsky, E. E. (2011). Collateral damage: Evolution with displacement of fracture distribution and secondary fault strands in fault damage zones. *Journal of Geophysical Research*, *116*(B3), B03405. https://doi.org/10.1029/2010JB007665

Schlische, R. W., Young, S. S., Ackermann, R. V, & Gupta, A. (1996). Geometry and scaling relations of a population of very small rift: related normal faults. *Geology*, *24*(8), 683–686. https://doi.org/10.1130/0091-7613(1996)024<0683:GASROA>2.3.CO;2

Scholz, C. H. (1987). Wear and gouge formation in brittle faulting. *Geology*, *15*(6), 493. https://doi.org/10.1130/0091-7613(1987)15<493:WAGFIB>2.0.CO;2

Scholz, C. H. (1998). A further note on earthquake size distributions. *Bulletin of the Seismological Society of America*, *88*(5), 1325–1326.

Scholz, C. H. (2019). *The mechanics of earthquakes and faulting* (Third edit). Cambridge university press.

Segall, P., & Pollard, D. D. (1980). Mechanics of discontinuous faults. *Journal of Geophysical Research*, *85*(B8), 4337. https://doi.org/10.1029/JB085iB08p04337

Sims, J. (1993). Chronology of displacement on the San Andreas fault in central California : Evidence from reversed positions of exotic rock bodies near Parkfield, California. In R. E. Powell, R. J. Weldon, & J. C. Matti (Eds.), *The San Andreas Fault System : Displacement, Palinspastic Reconstruction and Geologic Evolution*. Boulder, Colorado: Geological Society of America Memoir 178.

Stirling, M. W., Wesnousky, S. G., & Shimazaki, K. (1996). Fault trace complexity, cumulative slip, and the shape of the magnitude-frequency distribution for strike-slip faults: a global survey. *Geophysical Journal International*, *124*(3), 833–868. https://doi.org/10.1111/j.1365-246X.1996.tb05641.x

Sugiyama, Y., Fusejima, Y., Miyashita, Y., Kobayashi, K., & Miyawaki, A. (2005). Maturity and Activity of Faults in a Backarc Region of Southwest Japan Inferred From Integration of Topography, Paleoseismology, Coseismic Slip and Fault Rocks. *American Geophysical Union, Fall Meeting 2005, Abstract Id. T32B-07*.

Toké, N. A., Arrowsmith, J. R., Rymer, M. J., Landgraf, A., Haddad, D. E., Busch, M., et al. (2011). Late Holocene slip rate of the San Andreas fault and its accommodation by creep and moderate-magnitude earthquakes at Parkfield, California. *Geology*, *39*(3), 243–246. https://doi.org/10.1130/G31498.1

Valoroso, L., Chiaraluce, L., & Collettini, C. (2014). Earthquakes and fault zone structure. *Geology*, *42*(4), 343–346. https://doi.org/10.1130/G35071.1

Vermilye, J. M., & Scholz, C. H. (1998). The process zone: A microstructural view of fault growth. *Journal of Geophysical Research*, *103*(B6), 12223. https://doi.org/10.1029/98JB00957

Wakabayashi, J. (1999). Distribution of displacement on and evolution of a young system , California Sierra SN :, *18*(6), 1245–1274.

Waldhauser, F. (2009). Near-Real-Time Double-Difference Event Location Using Long-Term Seismic Archives, with Application to Northern California. *Bulletin of the Seismological Society of America*, *99*(5), 2736–2748. https://doi.org/10.1785/0120080294

Waldhauser, F., & Ellsworth, W. L. (2000). A Double-difference Earthquake location algorithm: Method and application to the Northern Hayward Fault, California. *Bulletin of the Seismological Society of America*, *90*(6), 1353–1368. https://doi.org/10.1785/0120000006

Waldhauser, F., & Schaff, D. P. (2008). Large-scale relocation of two decades of Northern California seismicity using cross-correlation and double-difference methods. *Journal of Geophysical Research: Solid Earth*, *113*(8), 1–15. https://doi.org/10.1029/2007JB005479

Wesnousky, S. G. (1988). Seismological and structural evolution of strike-slip faults. *Nature*. https://doi.org/10.1038/335340a0

Wilson, J. ., Chester, J. ., & Chester, F. . (2003). Microfracture analysis of fault growth and wear processes, Punchbowl Fault, San Andreas system, California. *Journal of Structural Geology*, *25*(11), 1855–1873. https://doi.org/10.1016/S0191-8141(03)00036-1

Yukutake, Y., & Iio, Y. (2017). Why do aftershocks occur? Relationship between mainshock rupture and aftershock sequence based on highly resolved hypocenter and focal mechanism distributions. *Earth, Planets and Space*, *69*(1), 68. https://doi.org/10.1186/s40623-017-0650-2

Figures and figure captions:

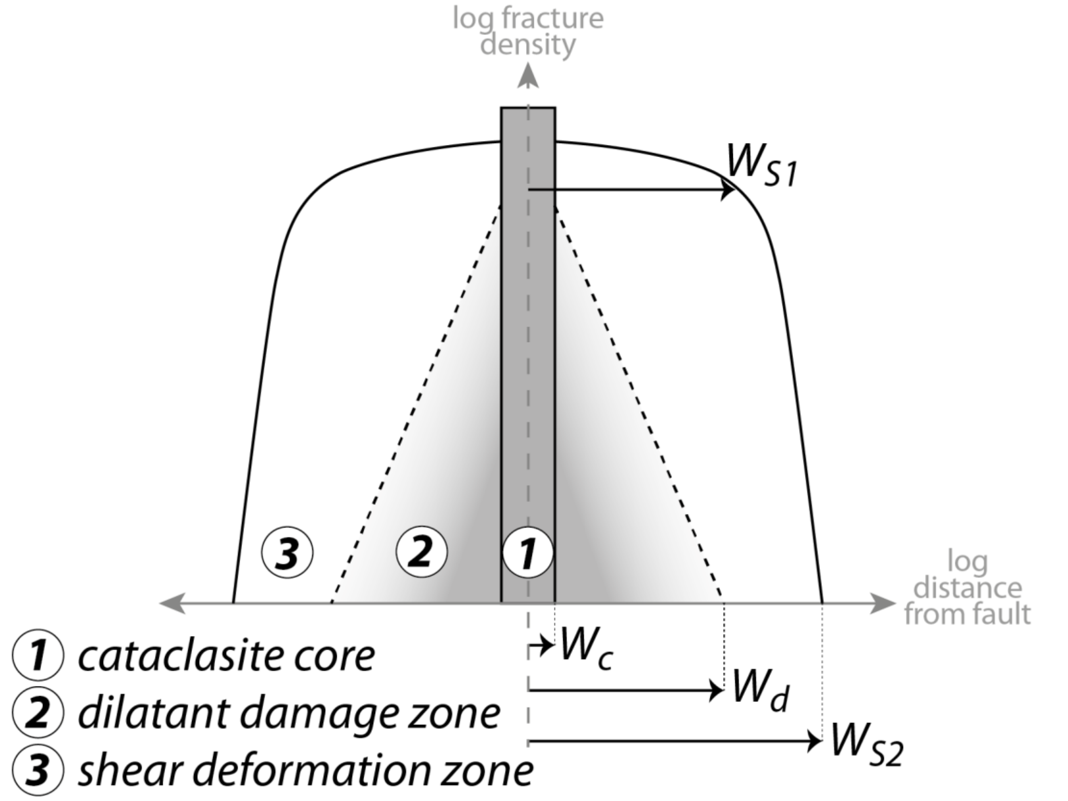

Figure 1; Perrin et al.

<u>Figure 1</u>: Simplified view of the architecture of a fault zone and the density of fractures and seismicity away from the fault core.

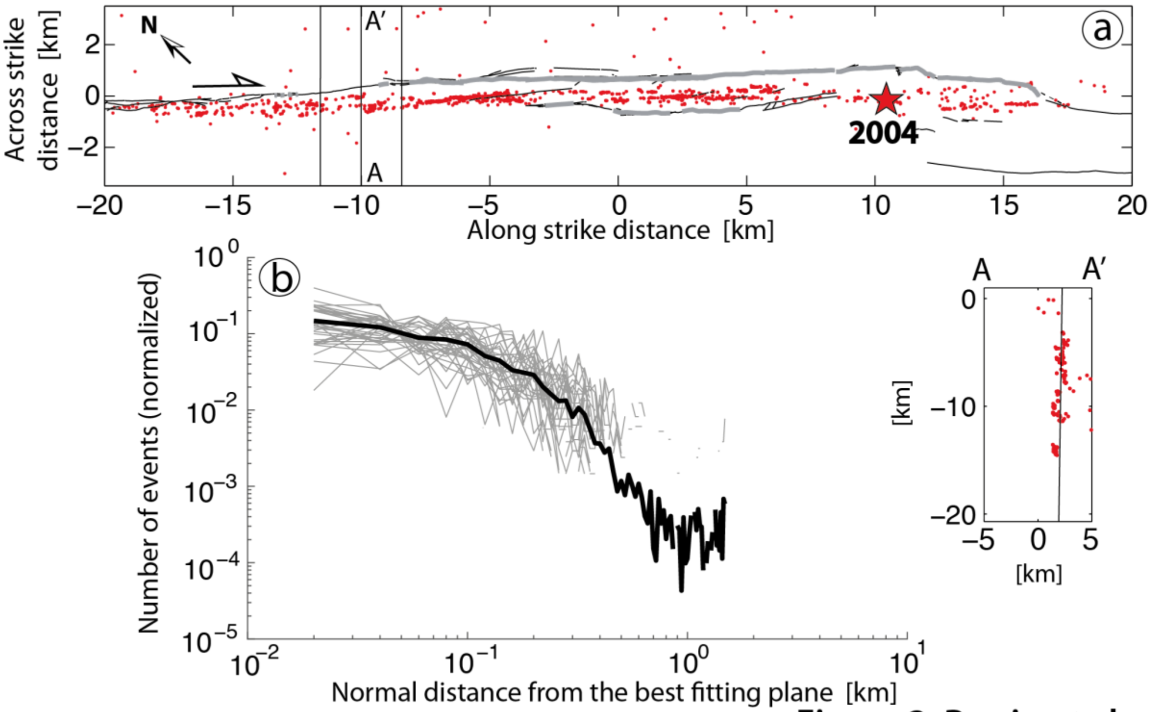

Figure 2; Perrin et al.

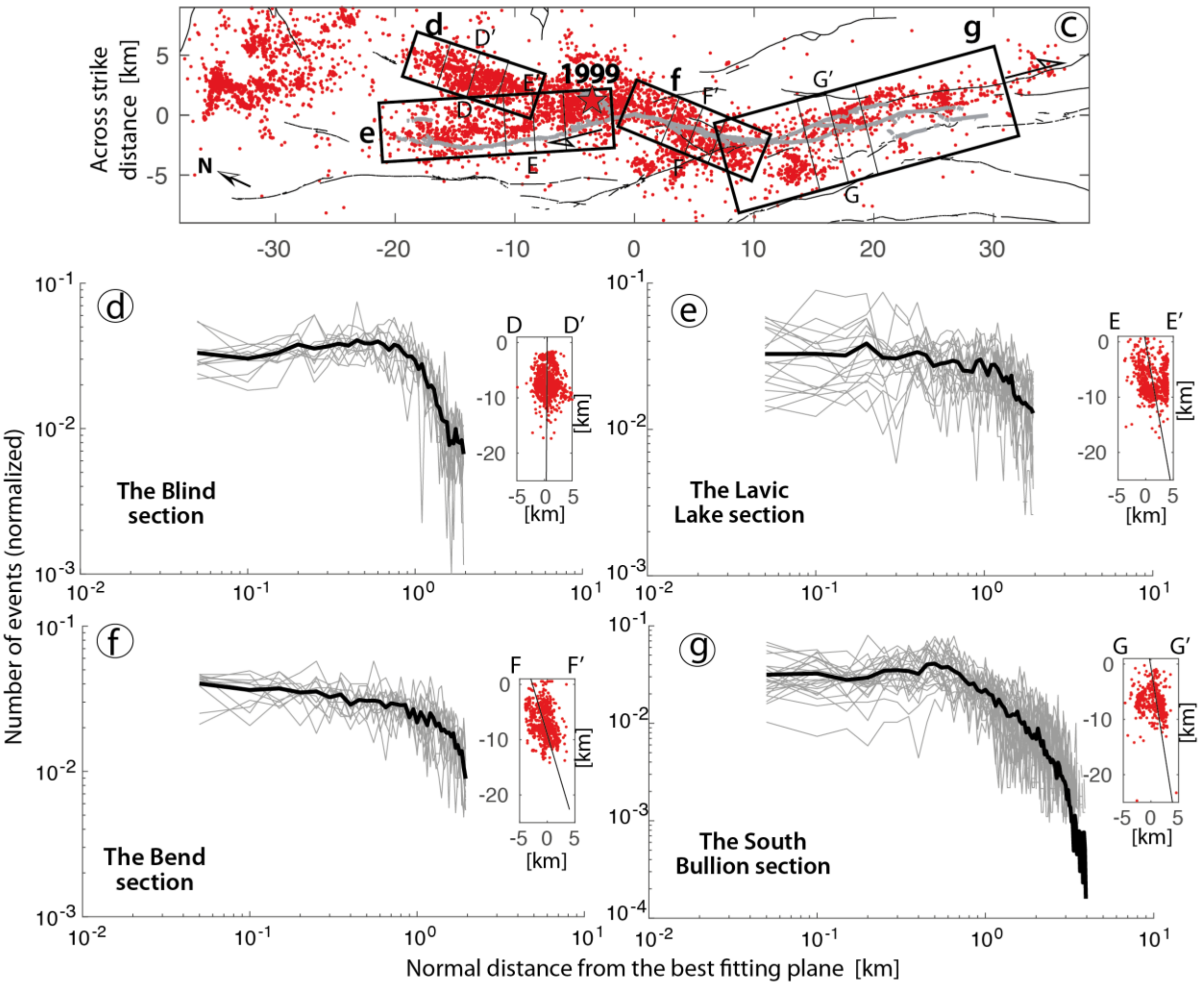

Figure 2 (following); Perrin et al.

<u>Figure 2</u>: Aftershocks distribution of the (a, b) 2004 Parkfield and (c, d, e, f, g) 1999 Hector Mine earthquakes (see Supp. Fig. 1 for all cases). (a) Map view showing the San Andreas fault (black lines) and the surface rupture (thick grey line) of the 2004 Parkfield earthquake (epicenter indicated by the red star). Red dots are aftershocks that occurred within 2 months after the mainshock (Waldhauser & Schaff, 2008; Perrin et al., 2019). (b) Gray profiles are fault-normal earthquake distributions measured from the best fitting plane in each moving box along the rupture trace. Black curves are the mean of the gray profiles. Inset: cross section going through the hypocenter area. Depth in y-axis; across strike distance in x-axis. Black line is best fitting plane minimizing fault-normal distance to aftershock hypocenters (red dots); (c) same as (a) but for the 1999 Hector Mine earthquake (earthquake catalog from Hauksson et al., 2012). Boxes include earthquakes used in d-g. (d-g) Same as (b) but for the 1999 Hector Mine earthquake. The four sub-figures are based on earthquakes included in boxes shown in (c).

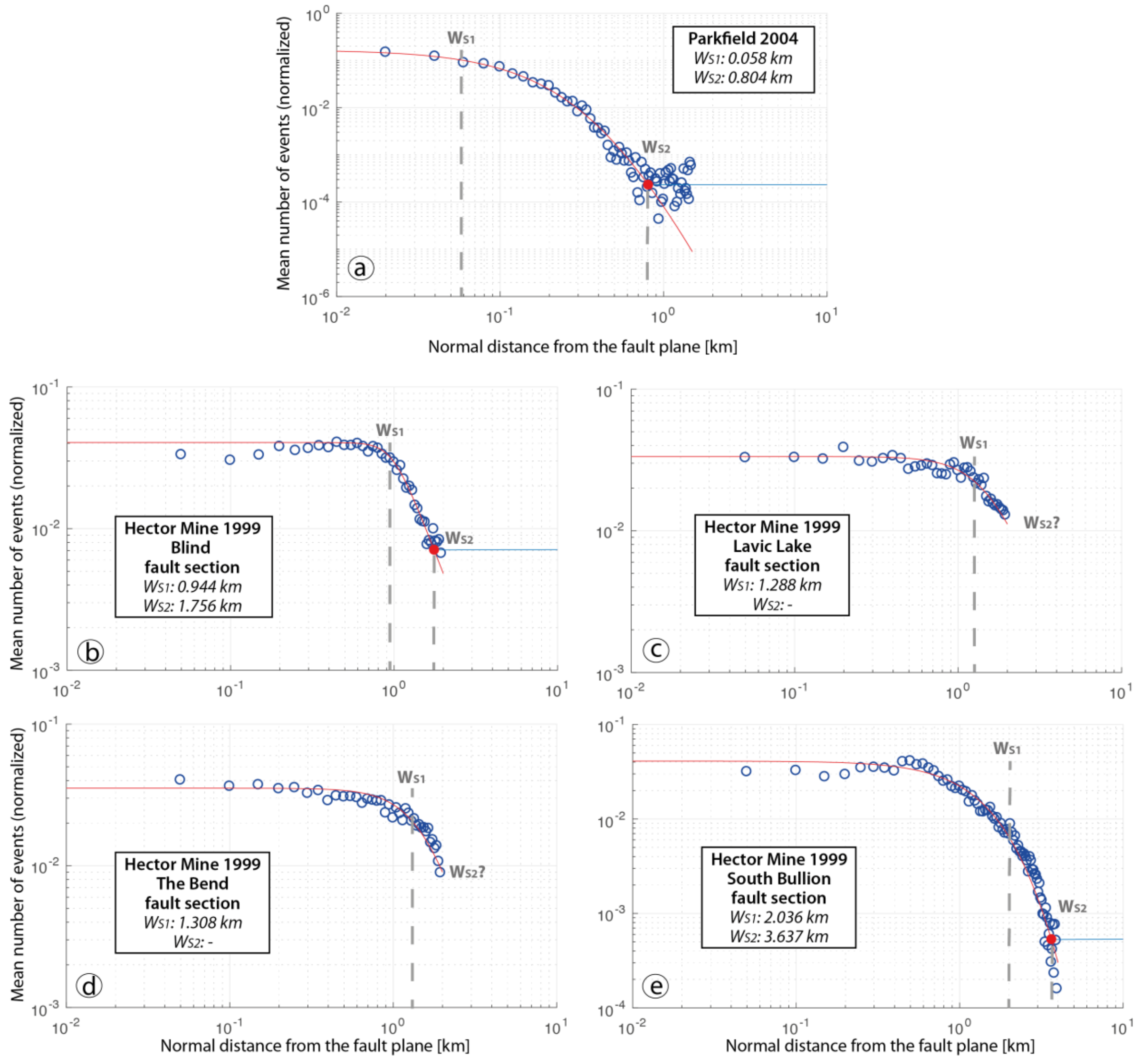

Figure 3 ; Perrin et al.

<u>Figure 3</u>: Determination of W_{S1} and W_{S2} parameters from the aftershocks distribution of the (a) Parkfield 2004 and (b, c, d, e) Hector Mine 1999 earthquakes (see Supp. Fig. 2 for all cases). Blue dots represent the mean distribution of each fault section (see black curve in Fig. 2 and Supp. Fig. 1). The red curve is the best fit of the distribution. The vertical gray dashed lines labeled W_{S1} and W_{S2} point out the locations where the numbers of earthquakes decrease rapidly and where they reach background level, respectively. W_{S1} is defined as the maximum of the 2[nd] derivative of the red fit. W_{S2} is defined by the red dot, which is the intersection between the red fit and the background level (horizontal blue line), when identified. .

Location	Earthquake name /date	Half width of seismicity fall off W_{S1} (km)	Half width of the shear deformation zone W_{S2} (km)	Name of fault section(s)	Initiation age (Ma)	Cumulative slip (km)	Long-term slip rate (mm/yr)	References for fault parameters
Japan	*Tottori, 2000*	*0.684 ±0.050*	*3.777 ±0.050*	*Komachi-Odani*	*~ 5*	*0.7 to 2.8†*	*~ 0.1*	Sugiyama et al., 2005 ; Active fault database of Japan*
USA	*El Mayor Cucapah, 2010*	*1.554 +1128/-0.702 (mean value)*	*6.335 ±1783 (mean value)*	*Elsinore (southern section)*	*~ 1.1*	*1 to 2*	*1 to 2*	Dorsey et al., 2012; K. E. K. Fletcher et al., 2011 and references therein
USA	*Hector Mine, 1999*	*1.394 +0.642/-0.302 (mean value)*	*2.697 ±940.5 (mean value)*	*Lavic Lake-Bullion*	*< 10*	*10 to 20*	*~ 0.8*	Dibblee, 1961; Dokka, 1983; Dokka & Travis, 1990; Garfunkel, 1974; Jachens et al., 2002; Oskin et al., 2007
USA	*Landers, 1992*	*0.954 +0.144/-0.254 (mean value)*	*3.736 ±0.050*	*Emerson-Camp Rock-Homestead Valley-Johnson Valley*	*< 10*	*3.5 to 4.6*	*0.2 to 0.7*	Dibblee, 1961; Dokka, 1983; Dokka & Travis, 1990; Garfunkel, 1974; Jachens et al., 2002; Rockwell et al., 2000; Rubin & Sieh, 1997
USA	*Morgan Hill, 1984*	*0.094 ±0.050*	*1.457 ±0.050*	*Calaveras*	*~ 12*	*60 to 70*	*3 to 25*	Stirling et al., 1996; Wakabayashi, 1999 and references therein
USA	*Parkfield, 2004*	*0.058 ±0.020*	*0.804 ±0.020*	*San Andreas (central section)*	*24 to 29*	*~ 315*	*~ 26*	Atwater & Stock, 1998; Critelli & Nilsen, 2000; Crowell, 1979; Graham et al., 1989; Liu et al., 2010; Matthews, 1976; Revenaugh & Reasoner, 1997; Toké et al., 2011
USA	*South Napa, 2014*	*0.268 ±50*	*0.907 ±0.050*	*West Napa (considered as part of the Calaveras fault zone)*	*~12*	*60 to 70*	*3 to 25*	Stirling et al., 1996; Wakabayashi, 1999 and references therein
USA	*Superstition Hills, 1987*	*0.858 ± 50*	*> 2.500*	*San Jacinto (southern section)*	*< 2*	*~ 4*	*~ 4*	Blisniuk et al., 2010; Dorsey et al., 2012; Gurrola & Rockwell, 1996; Hudnut & Sieh, 1989; Kirby et al., 2007; Lutz et al., 2006

New Zealand	-	*0.120 to 1.830 (field measurements)*	*~2800 (field measurements)*	*Awatere*	*< 4*	*< 2*	*~ 5*	Little, 1995 and references therein

<u>Table 1</u>: Fault and aftershock distribution parameters for the eight earthquake sequences analyzed in this study. Minimum uncertainties are defined by the bin of normal distribution in single earthquake cases. For multiple broken fault sections (Hector Mine, Landers, El Mayor Cucapah), W_{S1} and W_{S2} are mean values, when possible, and the uncertainties represent the minimum and maximum range of values (see detailed measurements in Supp. Figure S2). Field measurements of the Awatere fault from Little et al. (1995) are also indicated (for details see text).

* available at: https://gbank.gsj.jp/activefault/

† *deduced from scaling relations in* Schlische et al., 1996 *(see text for details)*

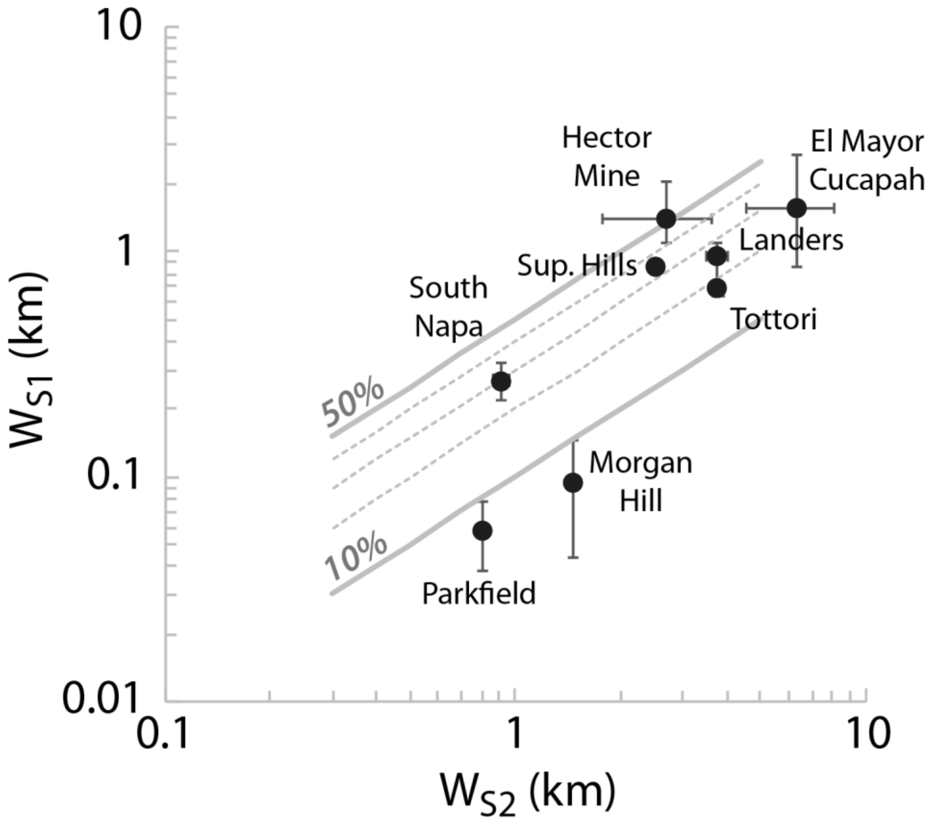

Figure 4; Perrin et al.

<u>Figure 4</u>: Relations between W_{S1} and W_{S2} for the eight earthquakes analyzed in this study.

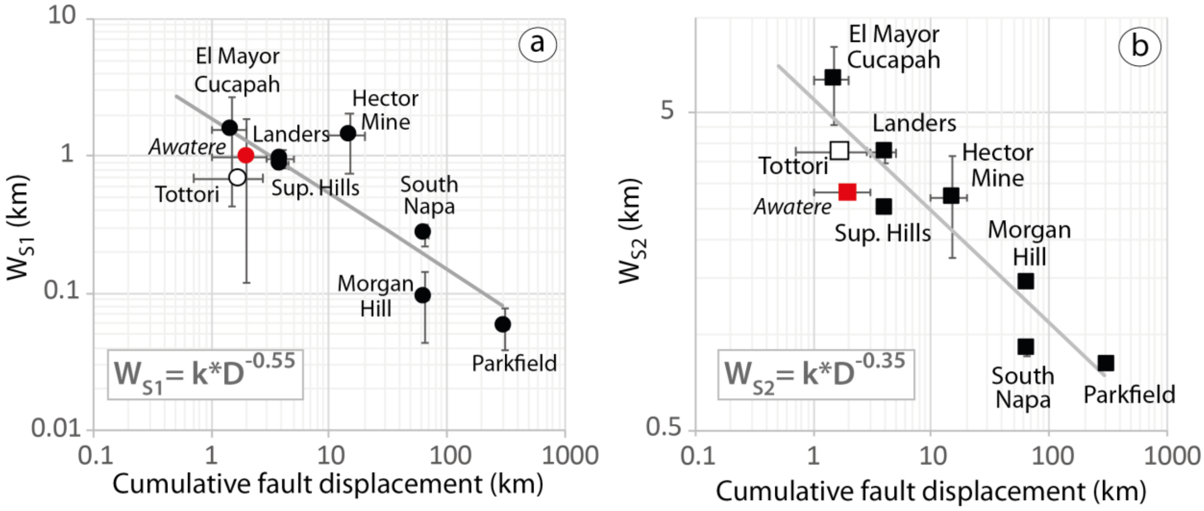

Figure 5; Perrin et al.

<u>**Figure 5**</u>**: Relations between (a) W_{S1} and (b) W_{S2} of eight earthquake sequences and the cumulative slip of their host fault taken from literature (solid symbols) and inferred (empty symbols)** (see Table 1 for details). Power laws are indicated by grey lines. For comparison, red symbols indicate geological surface measurements along the Awatere fault (from Little, 1995). D is the cumulative fault displacement, k is a constant.

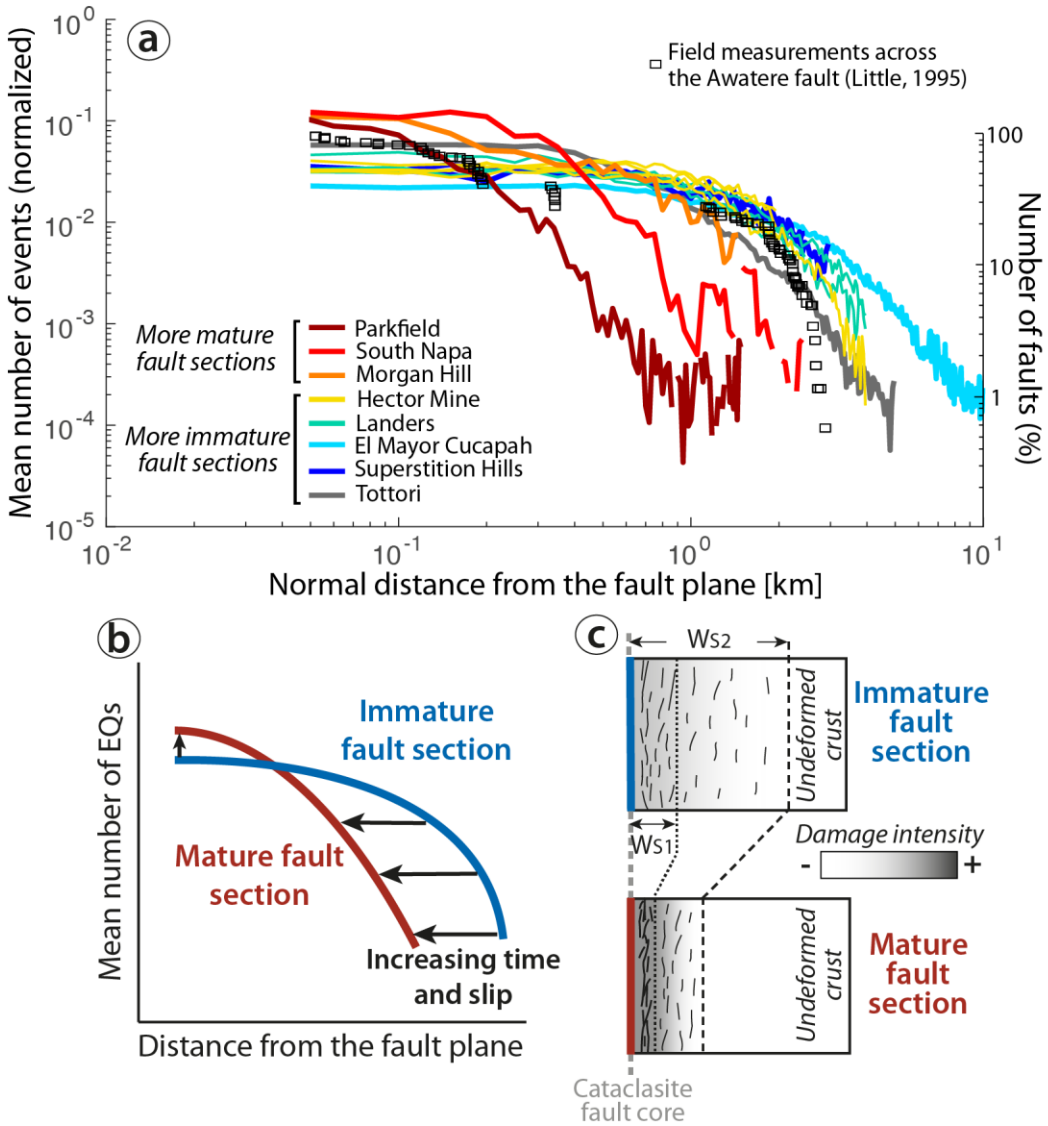

Figure 6; Perrin et al.

<u>**Figure 6**</u>: (a) **Normal distribution of the mean number of aftershocks as a function of distance from the fault, for the eight earthquake sequences analyzed in this study** (see also black curves in Fig. 2 and Supplementary Figure S1). Each colored curve represents one earthquake sequence. Curves with the same color are distinct fault sections that broke during one earthquake. Warm colors are more mature, cool colors more immature fault sections. For comparison, black squares indicate the cumulative number of faults (right *y* axis) measured at surface from the Awatere fault (modified from Little, 1995). (b) Sketch summarizing the fault-normal distributions of aftershocks for immature (blue curve) and mature (red curve) fault sections. (c) Interpretative

cross-section describing the structural makeup of immature (blue) and mature (red) faults. As fault structural maturity increases, then inner and outer bounds of the shear deformation zone (WS1 and WS2, respectively) decrease, as expressed by a decreasing width of the fault-normal aftershock distribution. See text for more discussion.

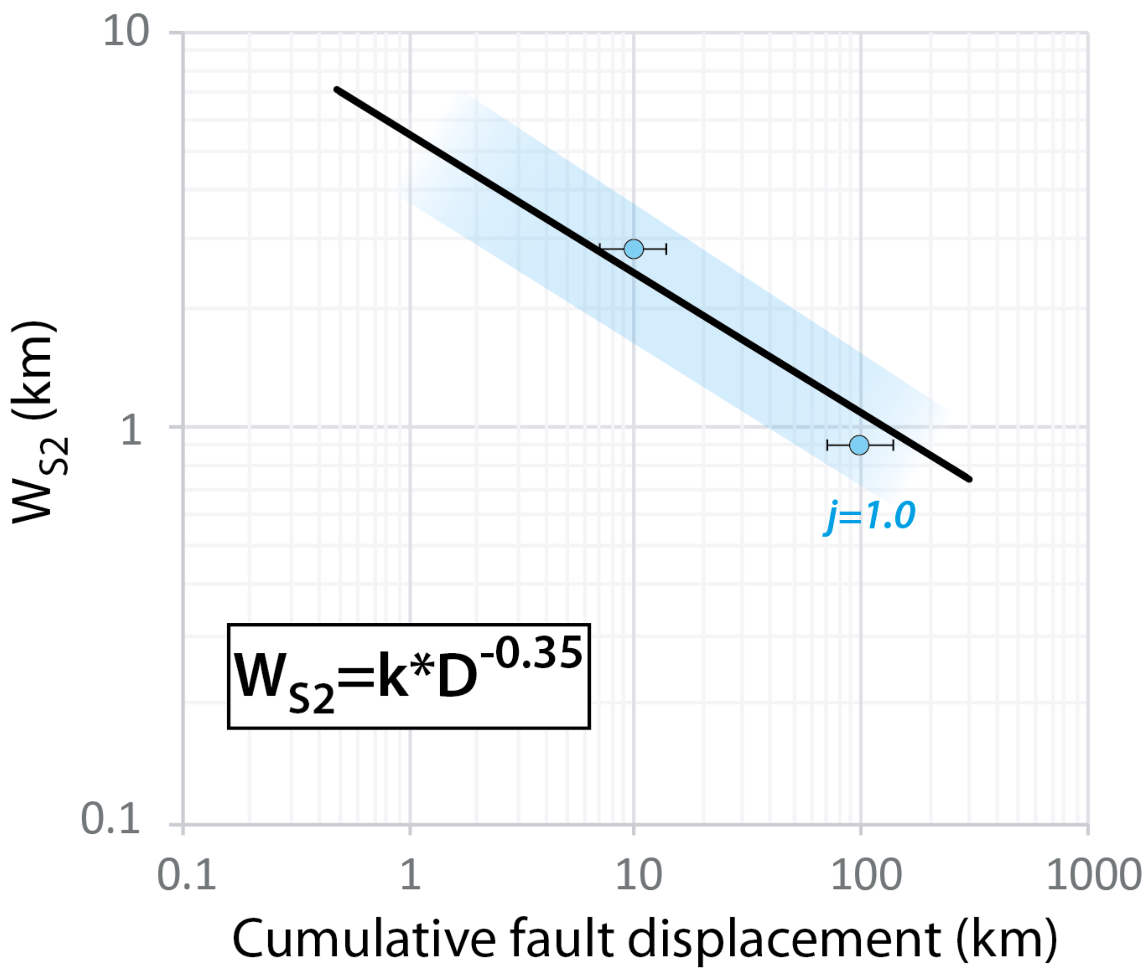

Figure 7; Perrin et al.

Figure 7: Comparison between power law deduced from the outer bound of the shear deformation zone (W_{S2}; black line) and power law built from observations and models in Stirling et al., 1996 and Aslam & Daub, 2018 (blue dots and shaded area). Blue dots are assuming typical jog heights j = 1 km, the blue shaded area bounds the blue dots assuming j=0.5 and 2 km.

Earthquake name	E_R (J)	M_0 (Nm)	E_R/M_0	$\Delta\sigma$ (MPa)	σ_a (MPa)	η_R (%)	References.
2000 Tottori	5.7e13	2.5e18	2.3e-5	23	0.7	6	Ross et al., 2018
1992 Landers	4e15	8e19	4e-5	11	1.7	25	J. B. Fletcher & McGarr, 2006
1999 Hector Mine	3e15	6e19	5e-5	6	1.5	50	Kaverina, 2002
2004 Parkfield	1.1e13	1e18	1.1e-5	2	0.3	25	Kim & Dreger, 2008; Ma et al., 2008

Table 2: Mainshock parameters for four earthquakes. E_R is radiated energy, E_G is the energy dissipated in damage of various types, $\Delta\sigma$ is stress drop, σ_a is apparent stress, M_0 is seismic moment, and η_R is the radiation efficiency.

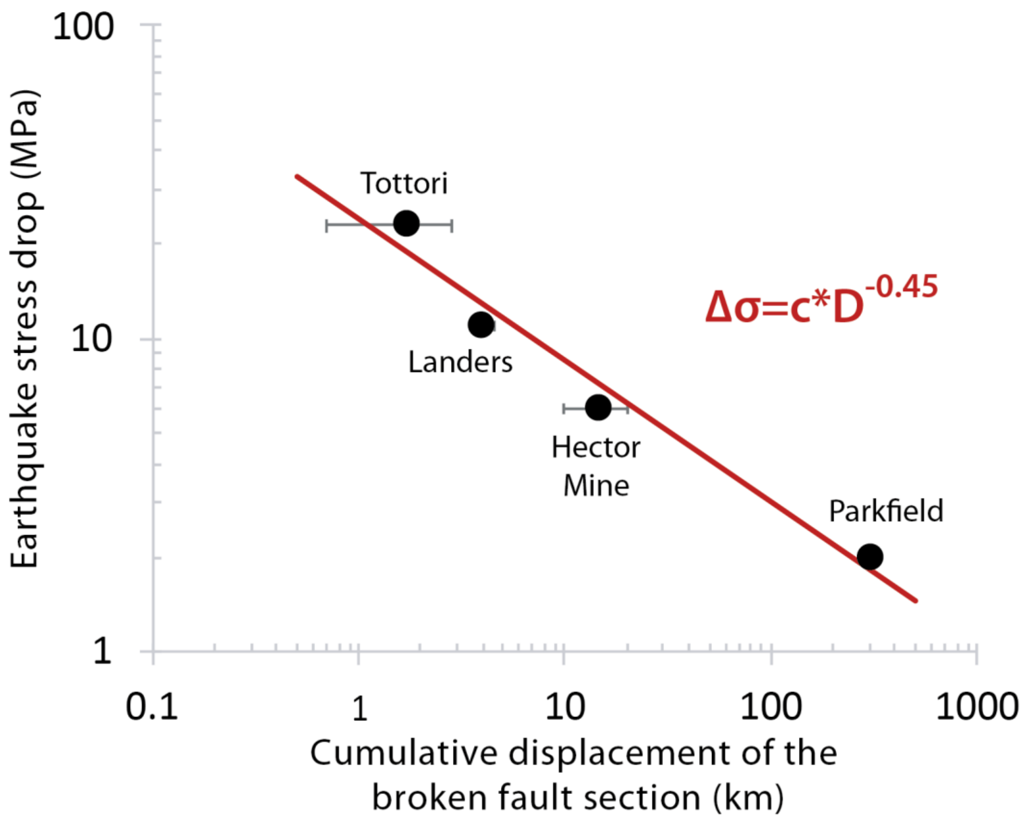

Figure 8; Perrin et al.

Figure 8: Earthquake stress drop ($\Delta\sigma$) as a function of cumulative displacement of the broken fault section (D) for earthquakes listed in Table 2. Parameter c is a constant.

AGU PUBLICATIONS

Journal of Geophysical Research

Supporting Information for

The Shear Deformation Zone and the Smoothing of Faults with Displacement

Clément Perrin[1,2,*], Felix Waldhauser[1] and Christopher H. Scholz[1]

[1] Lamont Doherty Earth Observatory at Columbia University, New York, USA

[2] Present address: Université de Paris, Institut de physique du globe de Paris, CNRS, F-75005 Paris, France

[*] **Corresponding author: perrin@ipgp.fr**

Contents of this file

Introduction

The Supporting Information includes two figures denoted Supplementary Figure S1 and S2 that provide the analysis of the across-strike aftershock distributions for the eight earthquake cases. Supplementary Figure S3 and S4 show other correlations between the size of the shear deformation zone determined from the aftershock distributions and independent geological parameters such as the initiation age and slip rate of the faults, respectively.

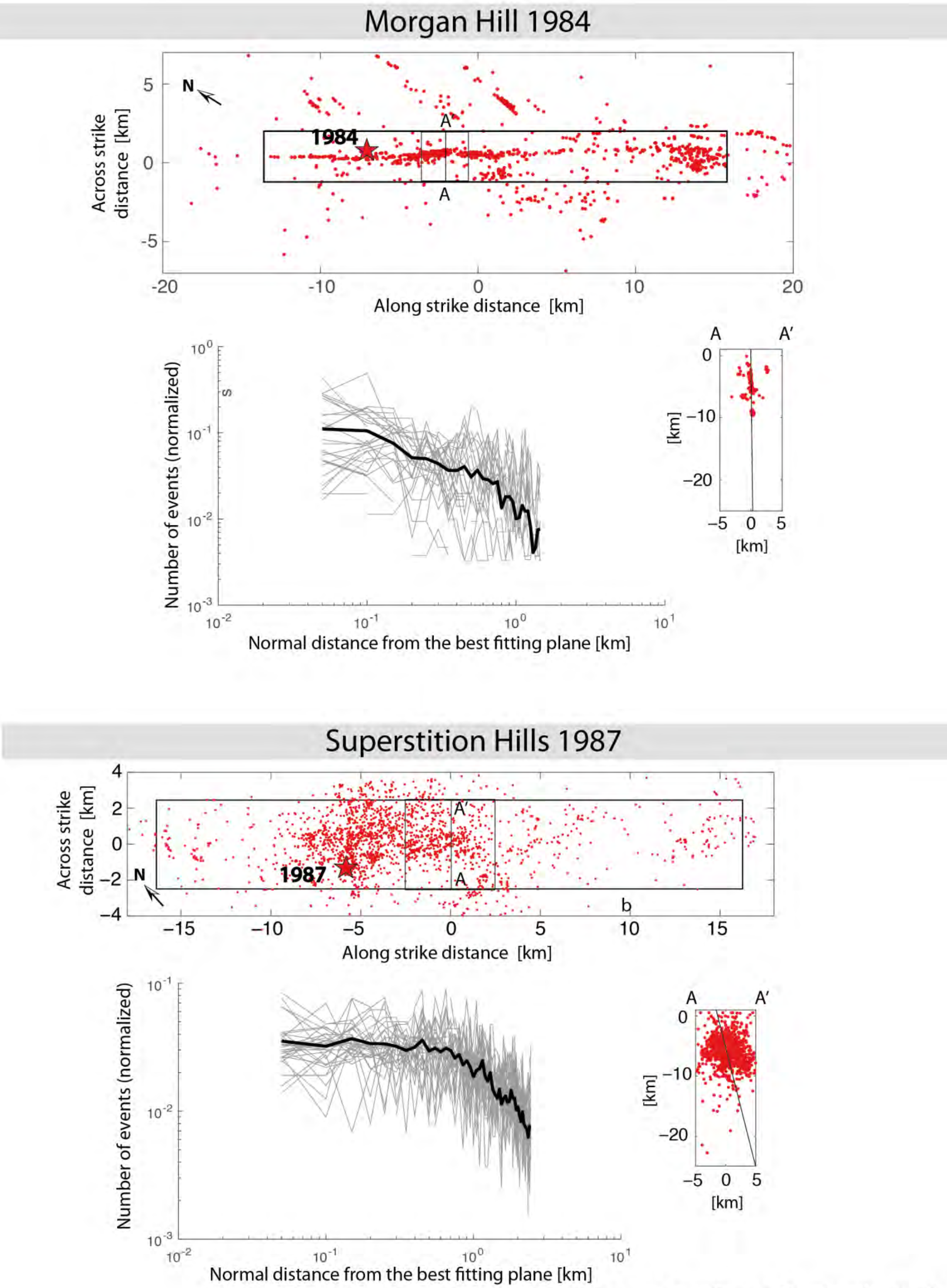

Supplementary Figure S1; Perrin et al.

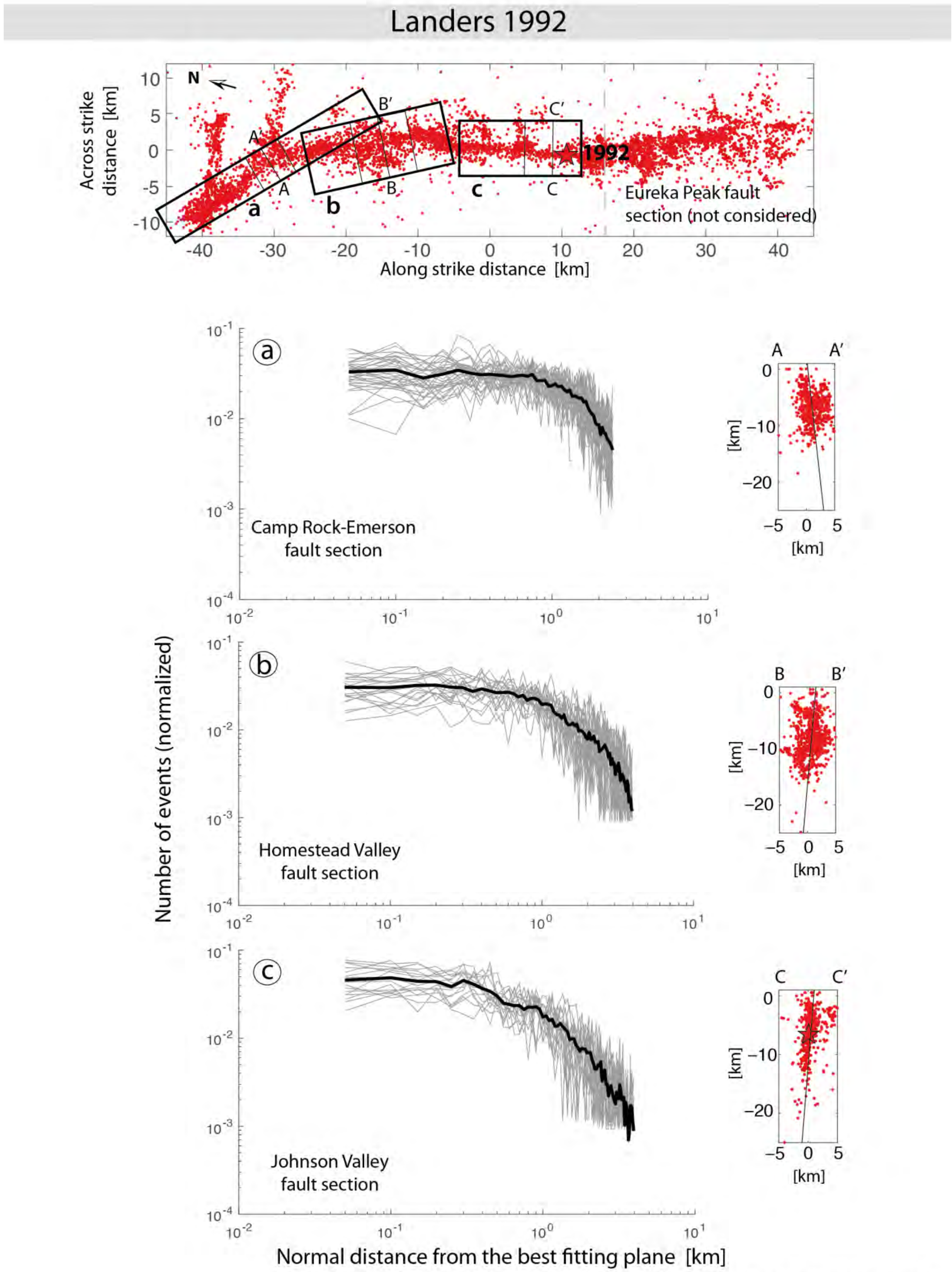

Supplementary Figure S1 (following); Perrin et al.

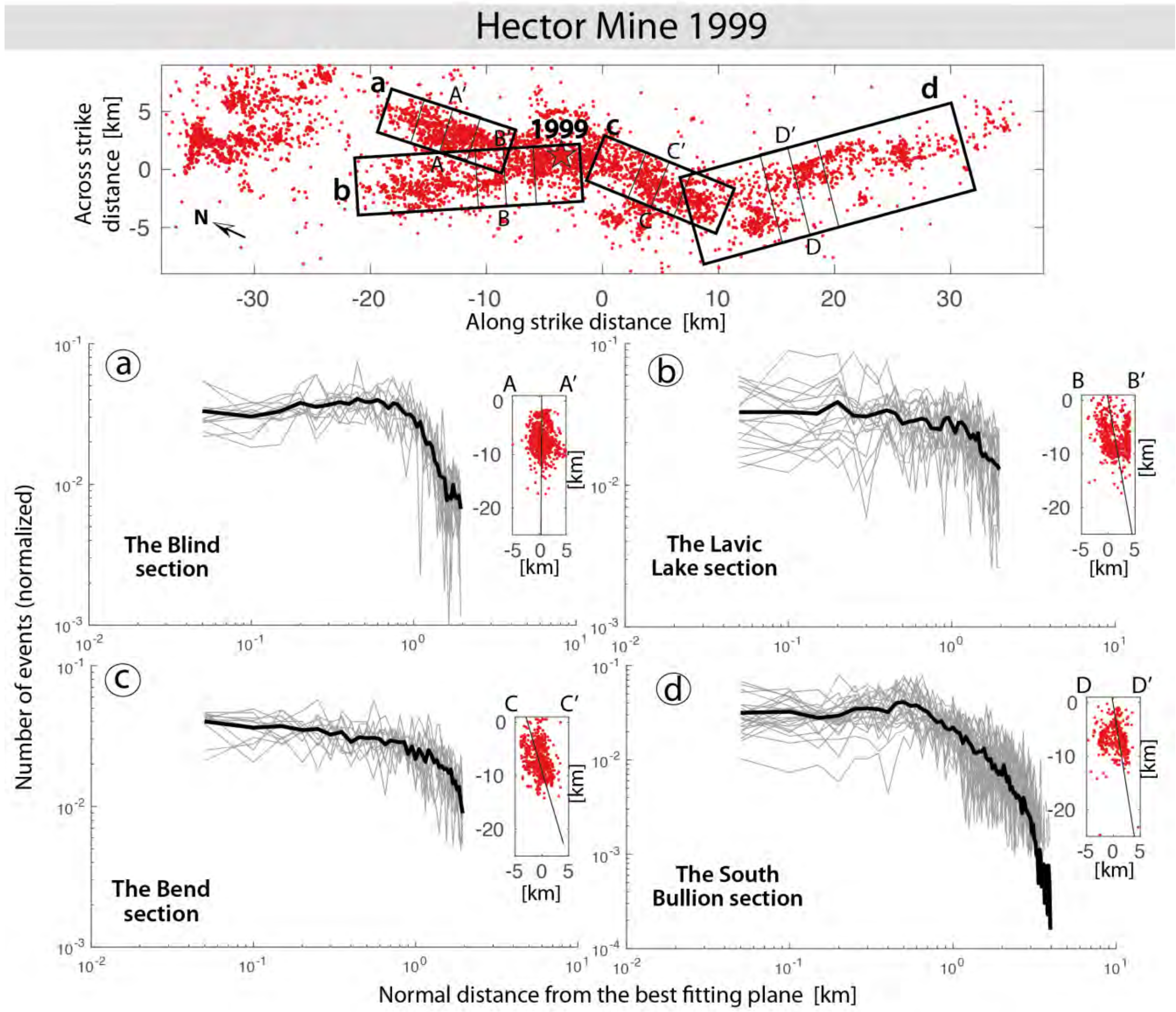

Supplementary Figure S1 (following); Perrin et al.

Tottori 2000

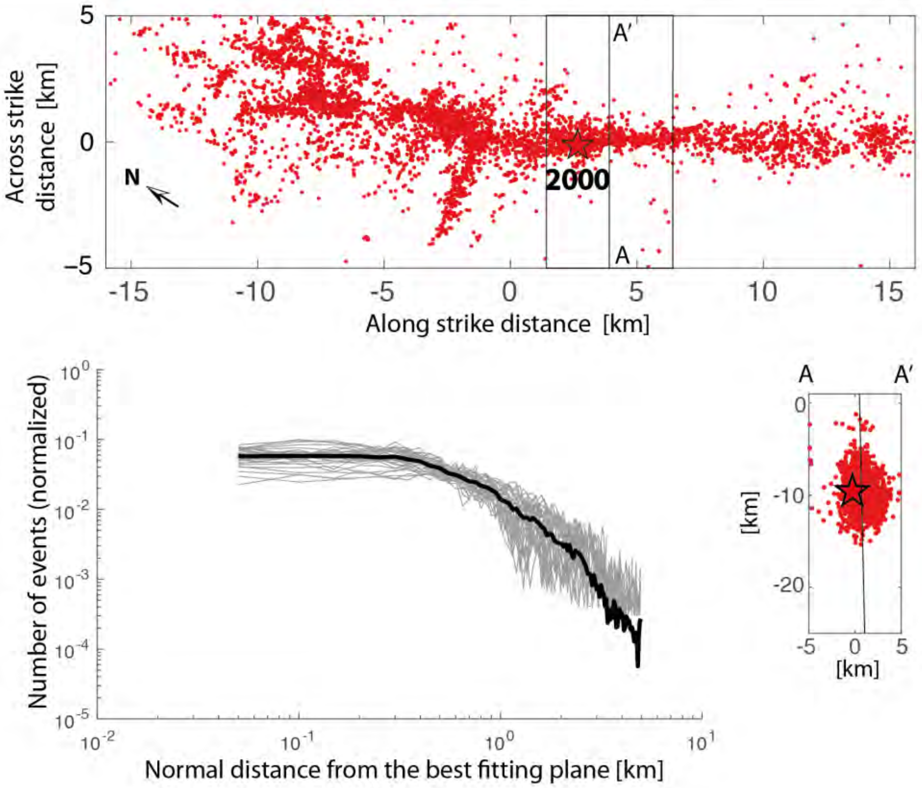

Parkfield 2004

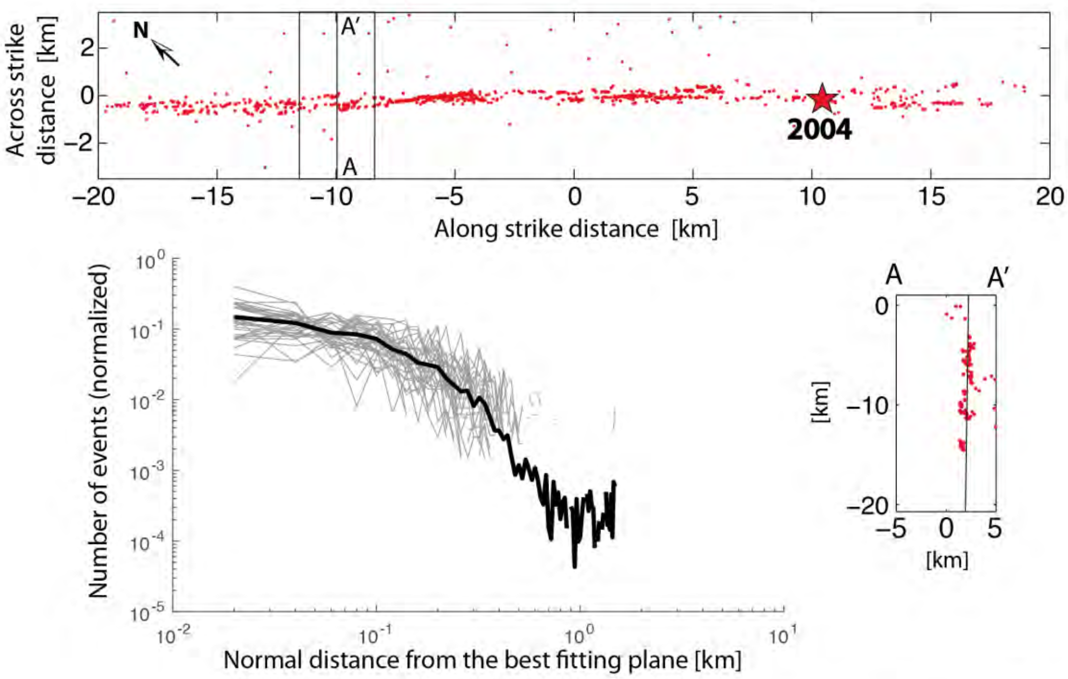

Supplementary Figure S1 (following); Perrin et al.

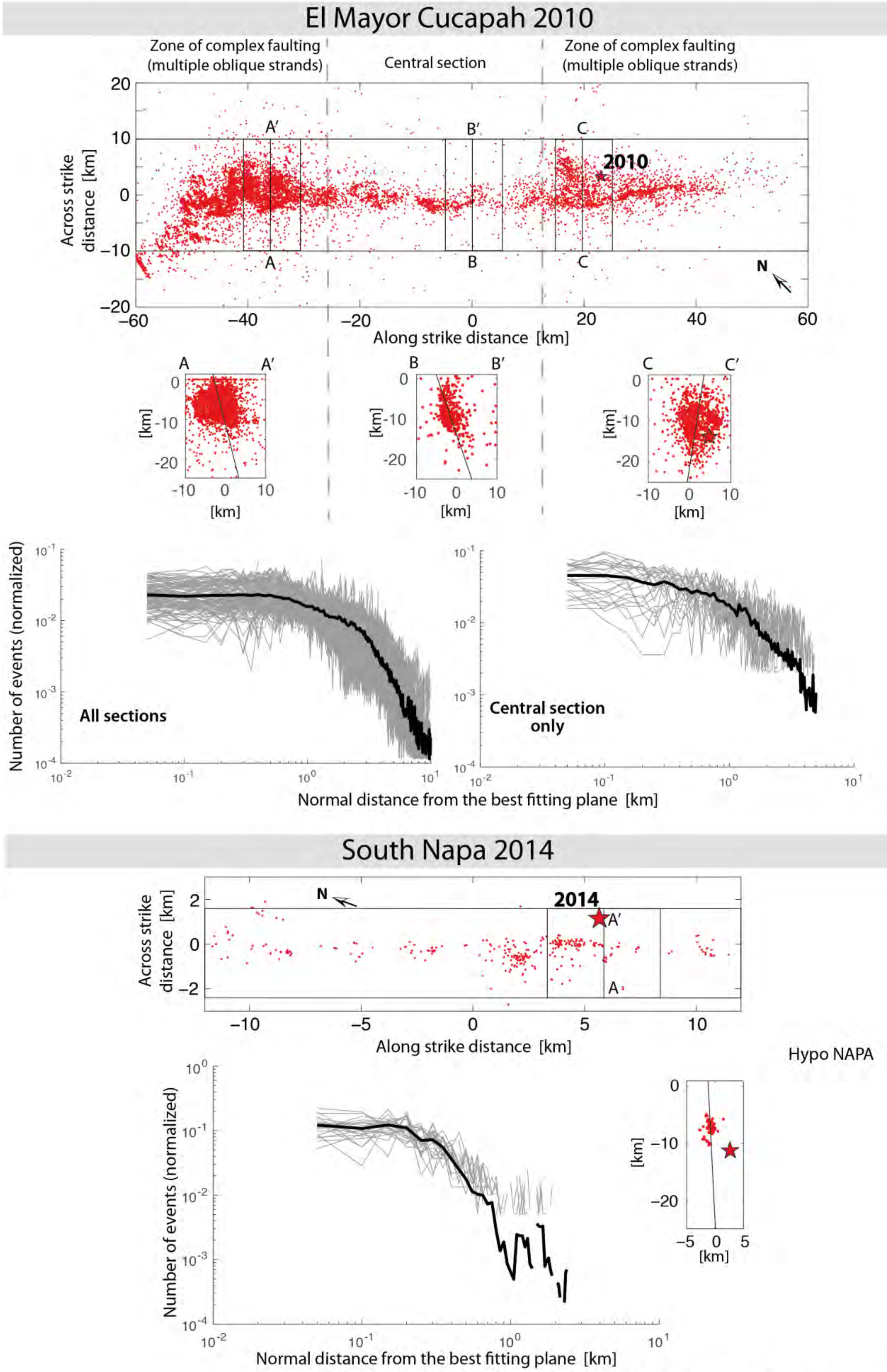

33 **Supplementary Figure S1 (following); Perrin et al.**

Supplementary Figure S1: Aftershock distributions of the eight earthquakes analyzed in this study (Morgan Hill 1984, Superstition Hills 1987, Landers 1992, Hector Mine 1999 Tottori 2000, Parkfield 2004, El Mayor Cucapah 2010 and South Napa 2014). (Top panels) Map view of the distribution of aftershocks (red dots) during the 2 months following the mainshock (red star) for each earthquake. If indicated, the thick black box shows the area selected to perform our analysis. (Bottom panels) Fault normal aftershock distribution (grey curves) measured from the best fitting plane in each box moving along the rupture trace. Black curves are the mean of the grey profiles. The small insets show selected cross sections going through the aftershock sequence (for locations see top panel). Depth in y-axis; across strike distance in x-axis. The black line is the plane best fitting the aftershocks using PCA (red dots).

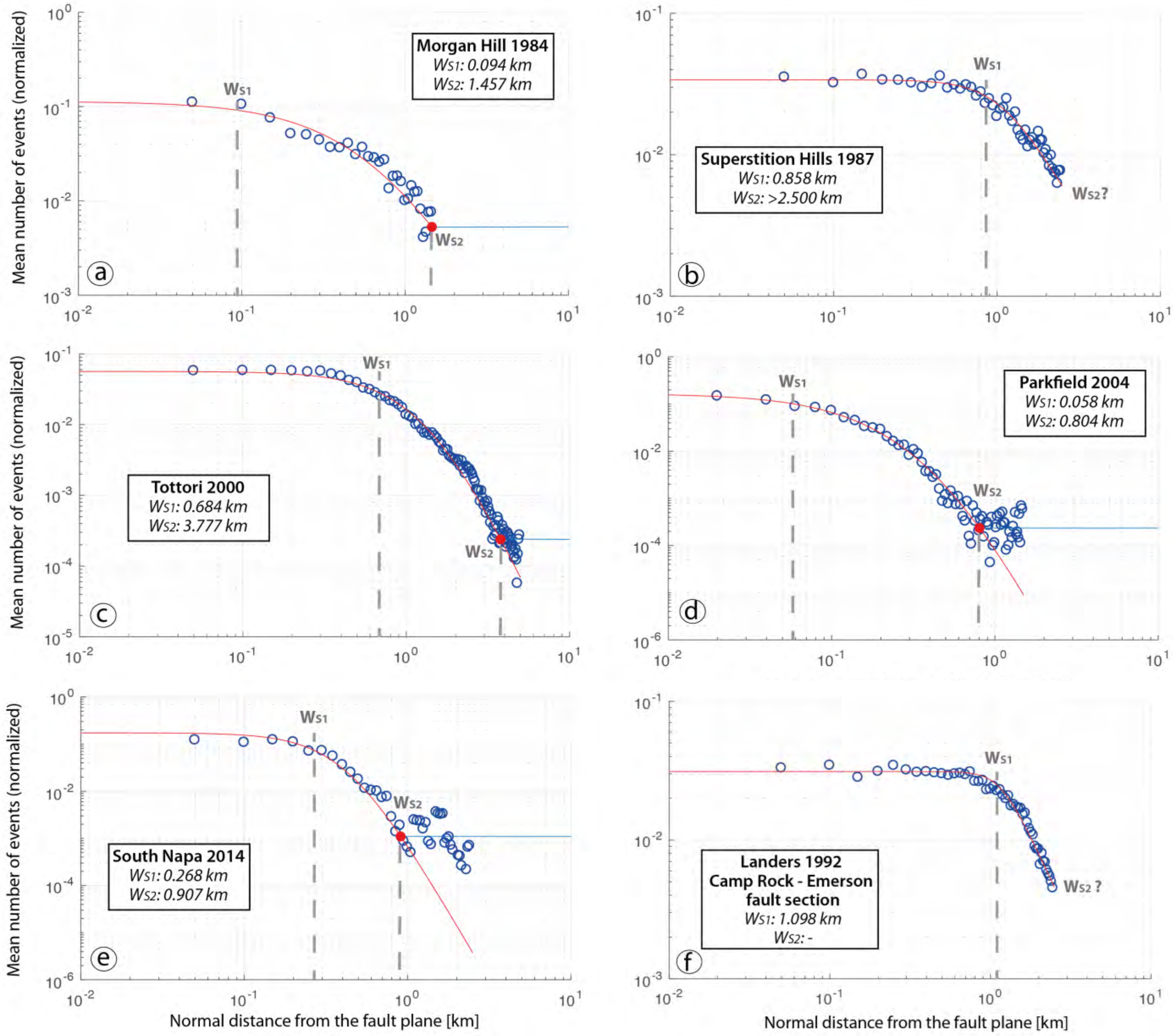
Morgan Hill 1984
Ws1: 0.094 km
Ws2: 1.457 km
Superstition Hills 1987
Ws1: 0.858 km
Ws2: >2.500 km
Tottori 2000
Ws1: 0.684 km
Ws2: 3.777 km
Parkfield 2004
Ws1: 0.058 km
Ws2: 0.804 km
South Napa 2014
Ws1: 0.268 km
Ws2: 0.907 km
Landers 1992
Camp Rock - Emerson
fault section
Ws1: 1.098 km
Ws2: -
Ws2?
Ws2 ?
Mean number of events (normalized)
Normal distance from the fault plane [km]
a
b
c
d
e
f

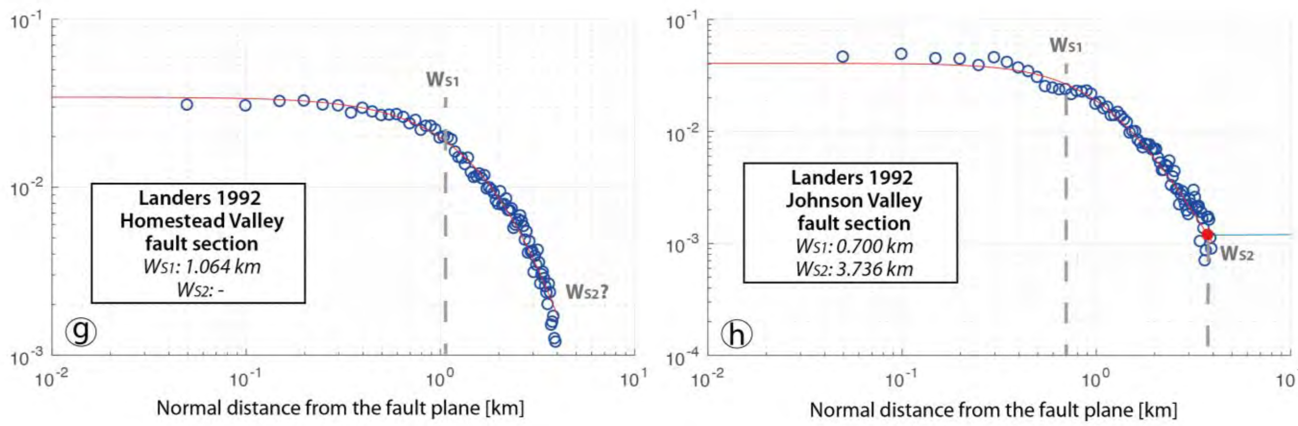
Landers 1992
Homestead Valley
fault section
Ws1: 1.064 km
Ws2: -
Ws2?
Landers 1992
Johnson Valley
fault section
Ws1: 0.700 km
Ws2: 3.736 km
Normal distance from the fault plane [km]
g
h

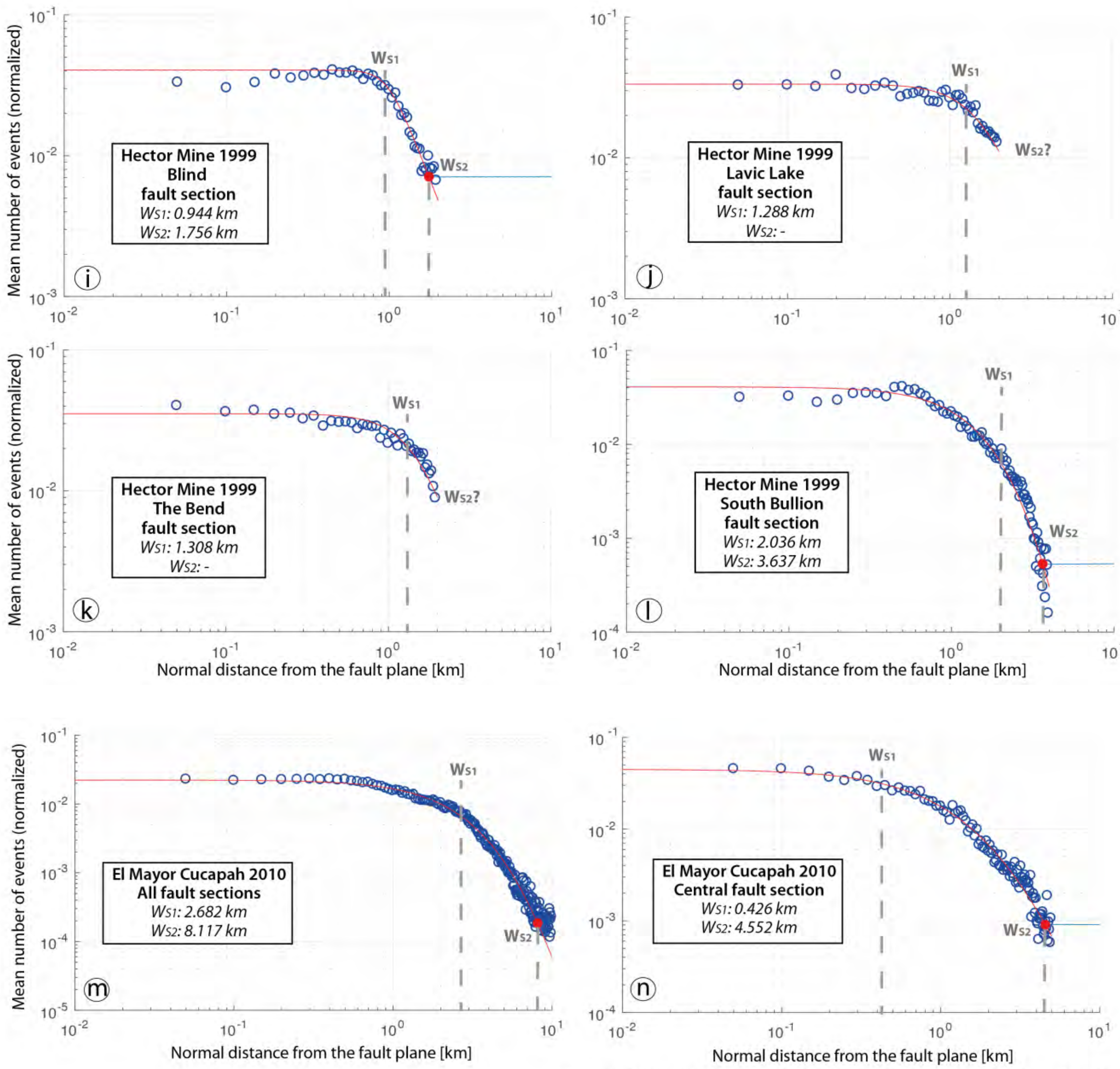

Supplementary Fig. 2 ; Perrin et al. (following)

<u>Supplementary Figure S2:</u> Determination of W_{S1} and W_{S2} parameters from the aftershock distribution of all earthquake cases: (a) Morgan Hill 1984 (b) Superstition Hills 1987 (c) Tottori 2000 (d) Parkfield 2004 (e) South Napa 2014, (f, g, h) Landers 1992 (i, j, k, l) Hector Mine 1999 (m, n) El Mayor Cucapah 2010. Blue dots represent the mean distribution of each fault section (see black curve in Supp. Fig. S1). The red curve is the best fit of the distribution. The vertical gray dashed lines labeled W_{S1} and W_{S2} point out the locations where the numbers of earthquakes decrease rapidly and where they reach background level, respectively. W_{S1} is defined as location where the maximum in the 2nd derivative is reached. W_{S2} is defined by the red dot, which is the intersection between the red fit and the background level (horizontal blue line).

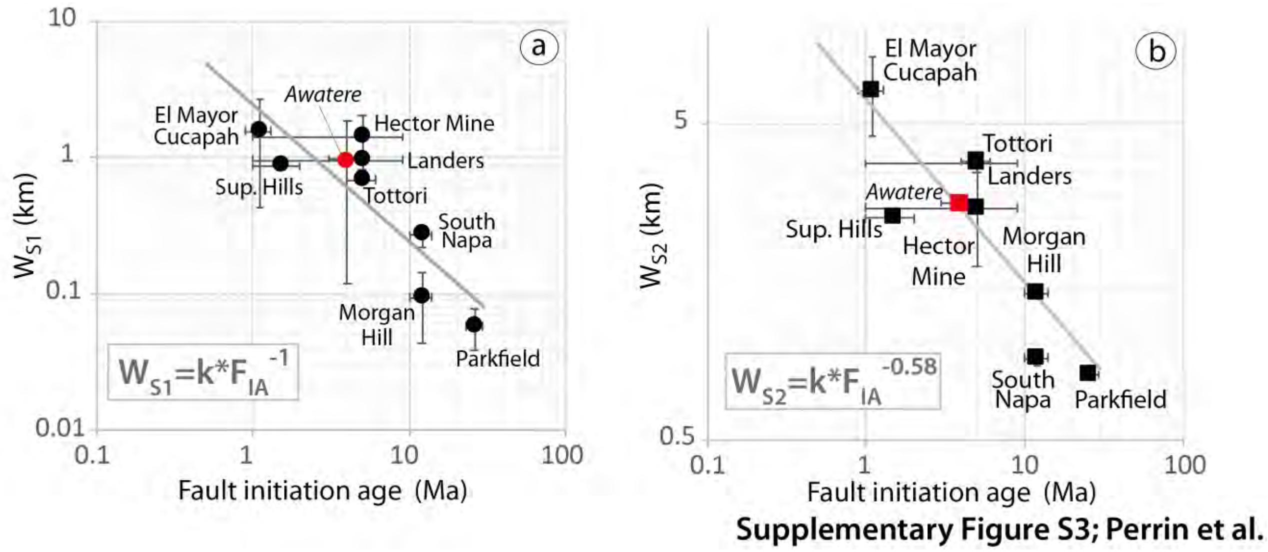

<u>Supplementary Figure S3:</u> Relations between (a) Ws1 and (b) Ws2 of the eight earthquake fault zones considered in this study and the fault initiation age. Power laws are indicated by grey lines. For comparison, red symbols indicate geological surface measurements along the Awatere fault (from Little, 1995).

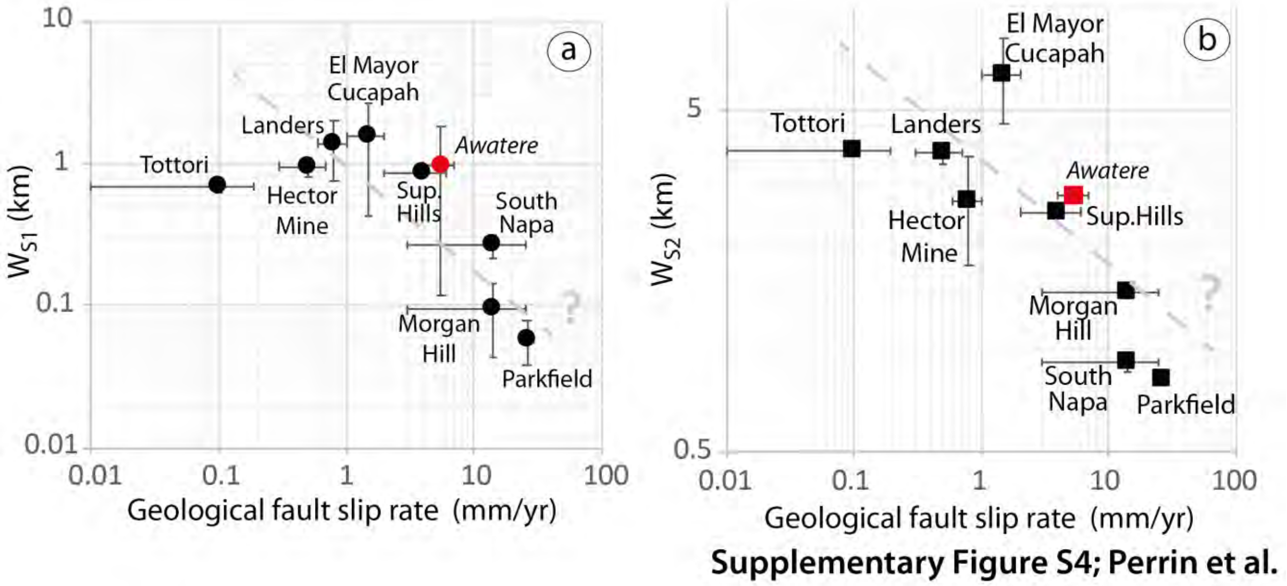

<u>Supplementary Figure S4:</u> Relations between (a) Ws1, (b) Ws2 of the eight earthquake fault zones considered in this study and the geological fault slip rate. Possible power laws are suggested by grey dashed lines. For comparison, red symbols indicate geological surface measurements along the Awatere fault (from Little, 1995).